Monthly Notices
of the
ROYAL ASTRONOMICAL SOCIETY

MNRAS **466,** 443–473 (2017)
Advance Access publication 2016 November 2

doi:10.1093/mnras/stw2811

New planetary systems from the Calan–Hertfordshire Extrasolar Planet Search

J. S. Jenkins,[1]★ H. R. A. Jones,[2] M. Tuomi,[2] M. Díaz,[1] J. P. Cordero,[1] A. Aguayo,[1] B. Pantoja,[1] P. Arriagada,[3] R. Mahu,[4] R. Brahm,[5] P. Rojo,[1] M. G. Soto,[1] O. Ivanyuk,[6] N. Becerra Yoma,[4] A. C. Day-Jones,[1] M. T. Ruiz,[1] Y. V. Pavlenko,[2,6] J. R. Barnes,[7] F. Murgas,[8] D. J. Pinfield,[2] M. I. Jones,[9] M. López-Morales,[10] S. Shectman,[11] R. P. Butler[3] and D. Minniti[12]

[1]*Departamento de Astronomia, Universidad de Chile, Casilla 36-D, Camino el Observatorio 1515, Las Condes, Santiago, Chile*
[2]*Center for Astrophysics, University of Hertfordshire, College Lane Campus, Hatfield, Hertfordshire AL10 9AB, UK*
[3]*Department of Terrestrial Magnetism, Carnegie Institution of Washington, 5241 Broad Branch Rd NW, 20015 Washington D.C., USA*
[4]*Department of Electrical Engineering, Universidad de Chile, Av. Tupper 2007, PO Box 412-3 Santiago, Chile*
[5]*Instituto de Astrofísica, Facultad de Física, Pontificia Universidad Católica de Chile, Av. Vicuña Mackenna 4860, Santiago, Chile*
[6]*Main Astronomical Observatory, Academy of Sciences of Ukraine, Golosiiv Woods, Kyiv-127, UA-03680, Ukraine*
[7]*Department of Physical Sciences, The Open University, Walton Hall, Milton Keynes MK7 6AA, UK*
[8]*Instituto de Astrofísica de Canarias, Via Lactea, E-38205 La Laguna, Tenerife, Spain*
[9]*Center of Astro-Engineering UC, Pontificia Universidad Católica de Chile, Av. Vicuña Mackenna 4860, Santiago, Chile*
[10]*Harvard–Smithsonian Center for Astrophysics, 60 Garden Street, Cambridge, MA 02138, USA*
[11]*Carnegie Institution of Washington, The Observatories, 813 Santa Barbara Street, Pasadena, CA 91101-1292, USA*
[12]*Departamento de Ciencias Fisicas, Universidad Andres Bello, Republica 220, Santiago, Chile*

Accepted 2016 October 28. Received 2016 October 25; in original form 2016 September 21

ABSTRACT

We report the discovery of eight new giant planets, and updated orbits for four known planets, orbiting dwarf and subgiant stars using the CORALIE, HARPS, and MIKE instruments as part of the Calan–Hertfordshire Extrasolar Planet Search. The planets have masses in the range 1.1–5.4 M_J's, orbital periods from 40 to 2900 d, and eccentricities from 0.0 to 0.6. They include a double-planet system orbiting the most massive star in our sample (HD147873), two eccentric giant planets (HD128356*b* and HD154672*b*), and a rare 14 Herculis analogue (HD224538*b*). We highlight some population correlations from the sample of radial velocity detected planets orbiting nearby stars, including the mass function exponential distribution, confirmation of the growing body of evidence that low-mass planets tend to be found orbiting more metal-poor stars than giant planets, and a possible period–metallicity correlation for planets with masses >0.1 M_J, based on a metallicity difference of 0.16 dex between the population of planets with orbital periods less than 100 d and those with orbital periods greater than 100 d.

Key words: planets and satellites: formation – stars: activity – stars: low-mass – planetary systems – stars: solar-type.

1 INTRODUCTION

After the discovery and confirmation of the hot Jupiter Dimidium (aka. Helvetios *b* or 51 Pegasi *b*) in 1995, our view of giant planets was changed forever. Giant planets orbiting dwarf stars like the Sun have been found to inhabit many regions of the parameter space. The first of these were found orbiting their stars with periods much shorter than those of Jupiter in our Solar system (e.g. Mayor & Queloz 1995; Marcy & Butler 1996). More recently as the number of giant planets has grown, a new population of *eccentric gas giants* has been shown to exist (e.g. Jones et al. 2006; Tamuz et al. 2008; Arriagada et al. 2010), making up a large fraction of the known systems, at least around main-sequence stars since the same high fraction does not appear to be present around giant stars (Jones et al. 2014). These planets seem to span the full range of masses from the sub-Jupiter range all the way up to the mass boundary between giant planets and brown dwarfs.

★ E-mail: jjenkins@das.uchile.cl

It has been thoroughly demonstrated that there is a clear bias to metal-rich stars hosting giant planets across the currently sampled range of orbital separations (Fischer & Valenti 2005; Sousa et al. 2011), a bias that seems to hold for stars beyond the main sequence (e.g. Reffert et al. 2015; Soto, Jenkins & Jones 2015; Jones et al. 2016). In comparison, recent work appears to show that stars that host lower mass planets have a metallicity distribution that is indistinguishable from those that host no known planets at all (Udry et al. 2007; Sousa et al. 2011; Jenkins et al. 2013b; Buchhave & Latham 2015). Furthermore, Jenkins et al. (2013b) suggest there exists a boundary that delimits a planet desert for the lowest mass planets in the metal-rich regime. Such results show that there is a fundamental relationship between the protoplanetary disc metallicity and the mass of planets that form in these discs, indicating further study of the planetary mass function and its relationship with metallicity is warranted.

Since metallicity plays a key role in the formation of the observed planetary systems, explained well by nature's merging of core accretion and planet migration (e.g. Ida & Lin 2004; Mordasini et al. 2012), and now we are reaching a population size where less obvious correlations can reveal themselves, studying the current population of known planets can provide a window into the fundamentals of planet formation and evolution for the stars nearest to the Sun.

In 2007, we started a radial velocity (RV) planet search programme on the HARPS instrument at La Silla Chile, with the goal of finding more gas giant planets orbiting supermetal-rich stars to increase the statistics, whilst also following up any discoveries to search for transit events. The first results from this work and the target sample were discussed in Jenkins et al. (2009) and since then our programme has expanded to make use of the CORALIE spectrograph (Jenkins et al. 2011a,b, 2013a). This paper announces the first planets from this survey detected using CORALIE and goes on to study the planet mass–metallicity plane to search for correlations between these two parameters.

In this work, we describe the latest efforts from our Calan-Hertfordshire Extrasolar Planet Search (CHEPS), which builds on previous work by this group. We include the new giant planets we have detected in this programme with the large sample of gas giants detected by RV measurements that already exist in the literature, in order to continue the search for emerging correlations that allow us a more stringent insight into the nature of these objects. In Section 2, we describe the measurements used in this work. In Section 3, we discuss the sample selection, introduce the new giant planet detections from this survey, and discuss some characteristics of their host stars. In Section 4, we perform tests of the mass function and its relationship to stellar metallicity, along with searching for correlations between these parameters and planetary orbital period and we briefly discuss the impact of these results. Finally, in Section 5 we summarize the main points of this work.

2 OBSERVATIONS AND REDUCTION

The RV data sets for these stars were observed using the precision RV spectrographs CORALIE, HARPS, and MIKE. Both the CORALIE and HARPS spectrographs are physically located at the ESO La Silla Observatory in Chile, where CORALIE is mounted on the Swiss Euler telescope and HARPS is fed by light from the ESO 3.6 m telescope. The MIKE spectrograph is located at the Las Campanas Observatory and is mounted on the Magellan Clay 6.5 m telescope.

In this work, 570 radial velocities are reported, with a fairly even split between CORALIE and HARPS observations, in comparison to the smaller fraction of MIKE data. The baseline of observations for the CORALIE data runs from 2009 November 25 until 2015 October 23 (BJD 2455160.53623−2457318.85147), whereas the HARPS data runs from 2007 May 28 until 2013 September 28 (BJD 2454248.60231−2456563.90982) showing that the HARPS data covers a longer baseline but the CORALIE data has better sampling coverage in general for these targets. The MIKE velocities run from 2003 August 13 until 2009 July 7 (BJD 2452864.57934−2455019.6938), covering a baseline of 6 yr that overlaps with the HARPS baseline but not the CORALIE data.

2.1 CORALIE

The analysis of CORALIE data involves the normal echelle reduction steps, such as debiasing the images using CCD bias frames, order location and tracing using polynomial fitting methods and aperture order filtering, pixel-to-pixel sensitivity correction (flat-fielding) by building a normalized master flat-field image and dividing out the master flat-field from the other images, scattered-light removal by measuring the contribution to the total light profile in the interorder regions, order extraction using a profile fitting method (Marsh 1989), and finally building a precise 2D wavelength solution that is good to $\sim$2.5 m s^{-1}overall precision (Jordán et al. 2014; Brahm & Jordan, in preparation). The final steps in the analysis include cross-correlating the individual spectra with a binary mask (either G2, K0, K5, or M2 depending on the spectral type of the star, see Baranne et al. 1996; Pepe et al. 2002) and fitting the cross-correlation function (CCF) with a Gaussian to measure the RV, along with the width of the CCF to generate realistic uncertainties. The instrumental drift is then measured and removed from the overall velocity by performing a second cross-correlation between the simultaneously measured Thorium-Argon (ThAr) lamp (simultaneously referring to observations where the second optical fibre illuminates the spectrograph with ThAr light) and a previously measured double ThAr observation where both fibres have been fed by light from the ThAr calibration lamp. These double ThAr measurements are generally taken every 1.5–2 h throughout the night to continually reset the wavelength solution zero-point. These steps were discussed in Jordán et al. (2014), however the overall performance in term of stability is shown in Appendix A.

An important additional step in the calculation of the radial velocities from CORALIE is the characterization of the offset between the data collected prior to the 2014 November upgrade of the instrument. As part of this upgrade, the CORALIE circular fibres were replaced with octagonal fibres to increase illumination stability, the double-scrambler was reintroduced into the system, and a focal mirror that focuses light on the guiding camera was replaced. Such instrumental upgrades are expected to introduce systematic offsets in the RV measurements compared to pre-upgrade observations.

In an attempt to account for the offset between the CORALIE reference velocities observed before and after the upgrade, we first determined this offset in our two RV reference targets, HD72673 and HD157347. We denote the mean estimate for the offset x_0 based on these reference targets as μ_0 and its standard error as σ_0. We then used these numbers to construct a prior probability for the offset x_1 in the first data set of our sample such that $\pi(x_1) = \mathcal{N}(\mu_0, \sigma_0^2)$. This prior probability was used to calculate a posterior for the offset and we denote the mean and standard deviation of this obtained posterior with μ_1 and σ_1, respectively. After that, we adopted the refined estimate of the offset of $\mu_i \pm \sigma_i$ to construct the prior probability for

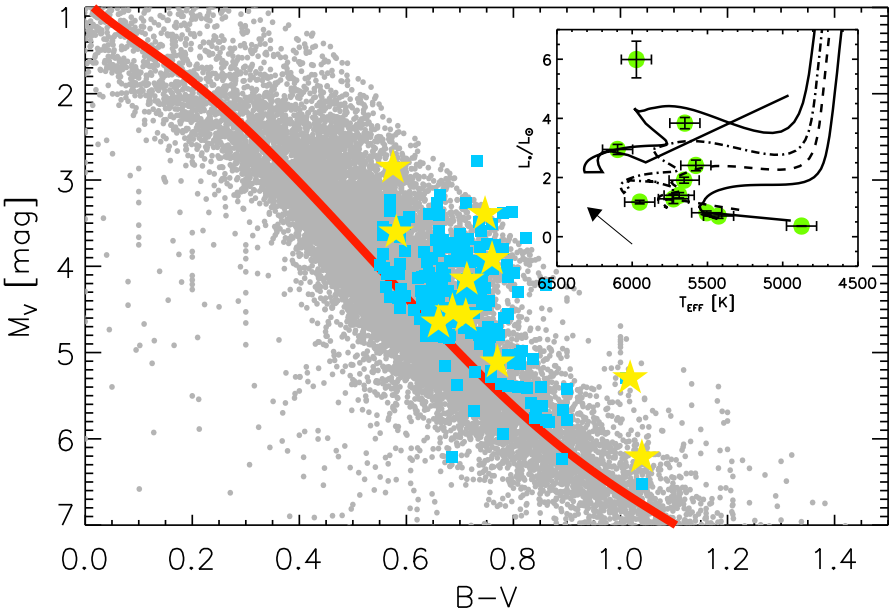

Figure 1. Positions of these stars on a colour–magnitude diagram. The grey filled circles are nearby stars drawn from the *Hipparcos* catalogue, the filled squares are the full sample of CHEPS targets, the filled stars are the positions of the stars discussed in this work, and the solid curve marks the position of the main sequence. In the inset, we show an HR-diagram with the positions of the stars discussed here, where the Y2 evolutionary models for masses of 1.0 (solid), 1.1 (dashed), 1.2 (dot–dashed), and 1.3 (dot–dot–dashed) and metallicities of +0.2 dex are shown increasing towards higher luminosities and temperatures. The arrow shows the approximate direction of increasing mass.

the offset x_{i+1} in the next data set, such that $\pi(x_{i+1}) = \mathcal{N}(\mu_i, \sigma_i^2)$. This process, called 'Bayesian updating' because the prior is updated into a posterior density that is in turn used as the next prior, was repeated until all the data sets were analysed. This process helps to account for all the information regarding the offsets from all the data sets without having to analyse them simultaneously. As a result, we summarize the information regarding the offset as a probability distribution that is almost Gaussian in the sense that the third and fourth moments are very close to zero. This density has a mean of 19.2 ms^{-1} and a standard deviation of 4.8 ms^{-1}, which indicates that an offset in the reference velocity of roughly 20 ms^{-1} is significantly present in the CORALIE data sets after the upgrade for the stars included in this work.

2.2 HARPS

For HARPS, the steps are similar to those mentioned above, but the data is automatically processed by the HARPS-DRS version 3.5 which is based in general on the procedure explained in Baranne et al. (1996). The nightly drift of the ThAr lines are found to be below 0.5 m s^{-1} and including the other sources of uncertainty such as centring and guiding (<30 cm s^{-1}), a stability of less than 1 m s^{-1} is found for this spectrograph over the long term (see Lo Curto et al. 2010).

2.3 MIKE

For the radial velocities measured using the MIKE spectrograph, the reduction steps are similar but the analysis procedure is different. MIKE uses a cell filled with molecular iodine (I2) that is placed directly in the beam of light from the target star before entering the spectrograph, and this is used to record the instrument point spread function (PSF) and provide a highly accurate wavelength fiducial. The full analysis procedure is explained in Butler et al. (1996), but in short, the velocities are measured by comparing each star+I2 spectrum to that of a template measurement of the same star. This template is observed without the I2 cell in place, such that one can deconvolve the instrument's PSF from the template observation, usually accomplished by observing a rapidly rotating B-star with the I2 cell in place before and after the template observation and extrapolating the PSF from these observations to that of the template. The deconvolved template can then be used to forward model each observation by convolving it with a very high resolution and high S/N I2 spectrum and a modelled PSF. The final stability of MIKE is found to be between that of CORALIE and HARPS, around the 5 m s^{-1} level of velocity precision.

3 THE STARS AND THEIR DOPPLER SIGNALS

The selection of the CHEPS target sample is discussed in Jenkins et al. (2009) but we outline the main selection criteria here. The stars are generally selected to be late-F to early-K stars, with a $B - V$ range between 0.5 and 0.9, and with a small number of redder stars included to allow the study of activity correlations and time-scales between activity indicators and the measured Doppler velocities. The positions of the CHEPS sample on a colour–magnitude diagram are shown in Fig. 1 (squares) compared to a general selection of nearby stars from the *Hipparcos* catalogue (circles), along with the targets discussed in this work (stars). The magnitude limits we set are between 7.5 and 9.5 in the V optical band and after preliminary screening with the FEROS spectrograph (Jenkins et al. 2008), we predominantly selected chromospherically quiet stars, and those that are metal-rich (primary sample having $\log R'_{\mathrm{HK}}$ indices ≤ -4.9 dex and [Fe/H] $\geq +0.1$ dex, with some stars outside of these selection limits to use as comparisons). The positions of the stars reported here on an HR-diagram are shown in the inset plot in Fig. 1. The Y2

Table 1. Stellar parameters for the hosts.

Parameter	HD9174	HD48265	HD68402	HD72892	HD128356	HD143361
Spectral type$_{Hipp}$	G8IV	G5IV/V	G5IV/V	G5V	K3V	G6V
$B - V_{Hipp}$	0.761 ± 0.002	0.747 ± 0.014	0.660 ± 0.021	0.686 ± 0.015	1.017 ± 0.015^{a}	0.773 ± 0.004
V	8.40	8.05	9.11	8.83	8.29	9.20
π (mas)	12.67 ± 0.62	11.71 ± 0.58	12.82 ± 0.61	13.74 ± 0.83	38.41 ± 0.77	15.23 ± 1.18
Distance (pc)	78.93 ± 3.86	85.40 ± 4.23	78.00 ± 3.71	72.78 ± 4.40	26.03 ± 0.52	65.66 ± 5.09
logR'_{HK}	-5.23	-5.24	-4.95	-5.03	-5.07	-5.12
Hipparcos N_{obs}	92	98	107	92	72	96
Hipparcos σ	0.014	0.009	0.017	0.016	0.013	0.016
ΔM_V	1.478	1.914	0.108	0.405	0.553	0.349
T_{eff} (K)	5577 ± 100	5650 ± 100	5950 ± 100	5688 ± 100	4875 ± 100	5505 ± 100
$L_\star/L_\odot$	2.41 ± 0.18	3.84 ± 0.19	1.17 ± 0.06	1.40 ± 0.09	0.36 ± 0.01	0.81 ± 0.06
$M_\star/M_\odot$	1.03 ± 0.05	1.28 ± 0.05	1.12 ± 0.05	1.02 ± 0.05	0.65 ± 0.05	0.95 ± 0.05
$R_\star/R_\odot$	1.67 ± 0.07	2.05 ± 0.05	1.02 ± 0.05	1.22 ± 0.06	0.85 ± 0.02	0.99 ± 0.08
[Fe/H]	0.39 ± 0.10	0.40 ± 0.10	0.29 ± 0.10	0.25 ± 0.10	0.17 ± 0.10	0.22 ± 0.10
log g	4.03 ± 0.05	3.92 ± 0.03	4.47 ± 0.05	4.27 ± 0.05	4.52 ± 0.06	4.42 ± 0.08
U,V,W (km s^{-1})	22.2,−56.5,−29	−14.2,−24.0,4.5	−37.5,−16.3,−17.3	72.2,−2.0,−15.8	30.8,−28.7,8.8	−24.4,−49.5,3.7
$v$sin i (km s^{-1})	2.1 ± 0.2	3.1 ± 0.3	2.9 ± 0.2	2.7 ± 0.2	1.3 ± 0.1	1.5 ± 0.1
Age (Gyr)	9 ± 3	5 ± 3	2 ± 3	8 ± 3	10 ± 5	5 ± 5
Parameter	HD147873	HD152079	HD154672	HD165155	HD224538	
Spectral Type$_{Hip}$	G1V	G6V	G3IV	G8V	F9IV/V	
$B - V_{Hip}$	0.575 ± 0.012	0.711 ± 0.025	0.713 ± 0.013	1.018 ± 0.095	0.581 ± 0.006	
V	7.96	9.18	8.21	9.36	8.06	
π (mas)	9.53 ± 0.99	12.00 ± 1.52	15.44 ± 0.84	15.39 ± 1.72	12.86 ± 0.73	
Distance (pc)	104.93 ± 10.90	83.33 ± 10.56	64.77 ± 3.52	64.98 ± 7.26	77.76 ± 4.41	
logR'_{HK}	-5.27	-4.99	-5.12	-5.18	-4.99	
Hipparcos N_{obs}	88	84	120	67	163	
Hipparcos σ	0.011	0.014	0.014	0.019	0.017	
ΔM_V	1.337	0.508	0.943	1.373	0.627	
T_{eff} (K)	5972 ± 100	5726 ± 100	5655 ± 100	5426 ± 100	6097 ± 100	
$L_\star/L_\odot$	5.99 ± 0.62	1.28 ± 0.16	1.91 ± 0.10	0.70 ± 0.08	2.95 ± 0.17	
$M_\star/M_\odot$	1.38 ± 0.05	1.10 ± 0.05	1.08 ± 0.05	1.02 ± 0.05	1.34 ± 0.05	
$R_\star/R_\odot$	2.29 ± 0.10	1.15 ± 0.13	1.44 ± 0.05	0.95 ± 0.11	1.54 ± 0.06	
[Fe/H]	-0.03 ± 0.10	0.16 ± 0.10	0.11 ± 0.10	0.09 ± 0.10	0.27 ± 0.10	
log g	3.86 ± 0.05	4.36 ± 0.10	4.15 ± 0.05	4.49 ± 0.11	4.19 ± 0.04	
U,V,W (km s^{-1})	18.7,−18.2,3.2	−39.6,−46.2,10.2	−20.0,−18.7,−29.1	13.3,9.8,−20.5	−29.1,−15.0,+7.2	
$v$sin i (km s^{-1})	5.9 ± 0.5	1.8 ± 0.1	2.2 ± 0.2	1.5 ± 0.1	3.9 ± 0.3	
Age (Gyr)	4 ± 3	3 ± 3	8 ± 3	11 ± 4	2 ± 3	

[a]Colour calculated from magnitudes drawn from the Tycho-2 catalogue (Høg et al. 2000).
We assign a standard $\pm$ 100 K uncertainty to the T_{eff} measurements and $\pm$ 0.10 dex to the metallicities.
π values come from van Leeuwen (2007) and all other *Hipparcos* parameters are taken from Perryman et al. (1997).
Evolutionary bulk properties and spectrally measured indices were either computed in this work or taken from Jenkins et al. (2008, 2011b) and Murgas et al. (2013).
[Fe/H] abundances, spectroscopic log g values, and rotational velocities were calculated using the procedures in Pavlenko et al. (2012) and taken from Ivanyuk et al. (2016).

isomass tracks are also shown (Demarque et al. 2004) for masses of 1.0–1.3 $M_\odot$, increasing in mass towards higher luminosities, and with a fixed metallicity of +0.2 dex. The characteristics of the targets we discuss in this work are shown in Table 1.

Since the planets reported here are gas giants, the RV signals of these stars are fairly large, and hence one might expect that we can detect frequencies for all of them using standard periodogram analyses to hunt for power peaks in the Fourier power spectrum, or minimum mean square error (MMSE) spectrum (e.g. Dawson & Fabrycky 2010; Jenkins et al. 2014). However, the search for the best solutions can be complicated, particularly for combined data sets from independent spectrographs because the sets have different baselines, data samplings, and uncertainties that all have to be accounted for in a search for periodic signals. The signals we discuss in this work are a mixture of well, and moderately well sampled data, such that some signals are more problematic to detect than others. Moreover, the inclusion of a linear trend that could be present in the data of a given target due to a long-period companion, will cause considerable correlations to the probability densities of the model parameters.

In Appendix B1, we show the MMSE power spectra for our sample of stars and it is clear that a number of deep troughs are present in the data, yet some sets show no significant power troughs over the frequency space searched. We thus applied the delayed-rejection adaptive-Metropolis algorithm (DRAM; Haario et al. 2006) together with tempered Markov chains when searching for solutions to our Keplerian models (see Tuomi 2014; Tuomi et al. 2014) and the simpler adaptive-Metropolis algorithm (Haario, Saksman & Tamminen 2001) when obtaining estimates for the model parameters. This method has previously been applied in Tuomi et al. (2013), Jenkins et al. (2013b,c), and Jenkins & Tuomi (2014), for example. The vertical dashed lines in

the MMSE periodograms mark the positions of these detected signals.

The DRAM algorithm works by using a sequence of proposal densities that are each narrower than the last. Here, 'narrower' is to be understood as a multivariate Gaussian proposal density, on which the adaptive-Metropolis algorithm is based, that has a smaller variance for at least one of the parameters in the parameter vector. In short, if a value proposed by drawing it from an initial proposal density is rejected, we continue by modifying the proposal density with respect to the period parameter(s) by multiplying it with a factor of 0.1 such that another value is proposed from a narrower area surrounding the current state of the chain. This enables us to visit the areas of high probability in the period space repeatedly and reliably and to see which periods correspond to the highest values of the posterior probability density.

We applied a statistical model that contains reference velocities of each instrument, a linear trend, Keplerian signals, and excess white noise. By simplifying the statistical model in Tuomi et al. (2014) by removing the intrinsic correlations that we do not expect to play a significant role due to the low number of measurements and the (relatively) high amplitude variations in the data, the model can be written as

$$m_{i,l} = \gamma_l + \dot{\gamma} t_i + f_k(t_i) + \epsilon_{i,l}, \quad (1)$$

where $m_{i,l}$ is the ith measurement made by the lth telescope/instrument, γ_l is the systemic velocity offset for each instrument, $\dot{\gamma}$ represents the linear trend, f_k is the superposition of k Keplerian signals at time t_i, and $\epsilon_{i,l}$ is a Gaussian random variable with zero mean and a variance of $\sigma_l^2 + \sigma_i^2$, where σ_l is a free parameter in our analyses that represents the stellar jitter noise and σ_i is the measurement uncertainty. We use prior probability densities as described in Tuomi (2012) but apply an informative prior density for the orbital eccentricities such that $\pi(e) \propto \mathcal{N}(0, 0.3^2)$ that penalizes, but does not exclude, eccentricities close to unity (Anglada-Escudé et al. 2013; Tuomi & Anglada-Escudé 2013). Therefore, given the previous tests performed using this model, in particular using high-precision HARPS data, we expect this model to represent a sufficiently accurate description of the velocities analysed in this work. The good agreement between the parameters published for the stars we discuss that overlap with previous work is testament to the model's applicability.

Posterior densities for the periods, semi-amplitudes, and eccentricities for all signals are shown in Appendices C1, C2, and C3, and below we discuss each of the systems independently. Note that all the signal fits are shown phase folded to highlight the phase coverage we have observed. We did not show the posteriors for the residuals to any of the systems (more than a single planet model fit) unless we detected a unique solution that relates to a second Doppler signal.

3.1 HD9174

HD9174 is classed as a G8 subgiant star in the *Hipparcos* catalogue (Perryman et al. 1997) since it has a distance from the main sequence (ΔM_V) of 1.5 and a $B - V$ colour of 0.76. The star is also extremely metal-rich, with an [Fe/H] of nearly +0.4 dex, indicating a high probability of hosting a giant planet. A signal with a semi-amplitude of 21 m s^{-1} has been detected with a period of nearly 1200 d. The star is very chromospherically quiet and exhibits low rotational velocity, indicating it is an ideal subgiant to search for orbiting exoplanets using the RV method, and hence we do not believe the signal is induced by activity features, and therefore conclude that HD9174 hosts an orbiting planet.

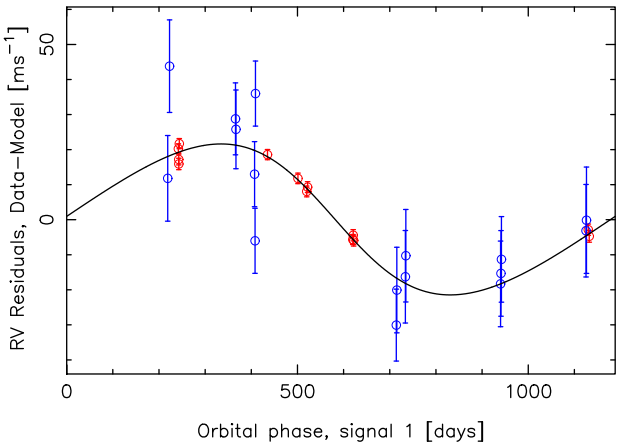

Figure 2. Phase folded CORALIE (blue) and HARPS (red) velocities for HD9174. The solid curve is the best-fitting Keplerian model.

In order to understand the significance of the detected signals we present here, we calculated log-Bayesian evidence ratios for each of the signals presented here based on the Markov Chain Monte Carlo (MCMC) samples drawn from a mixture of prior and posterior densities, as discussed in Newton & Raftery (1994, see equations 15 and 16). This is a version of importance sampling that uses a mixed distribution to obtain a sampling distribution that has 'heavier' tails than the posterior (see Nelson et al. 2016 for further discussion of this method). We note that all of these signals are so strong that they would pass essentially any meaningful significance test, from likelihood-ratio tests to tests applying any other information criteria.

The log-Bayesian evidence ratio for the signal in the data of HD9174 was found to be 42.1 for the one-planet model. The signal is also readily apparent in the MMSE periodogram. No secondary signal was detected. Considering we set the threshold boundary for a statistically significant signal to be at the level of 10^4, or 9.21 in log-Bayesian units, it is clear that this signal is very significant. Our best fit to the data yields a non-circular eccentricity, only at the level of around 0.12, and with a stellar mass commensurate with that of the Sun, the orbiting planet has a minimum mass of 1.11 M_J. The phase folded velocities and model fit are shown in Fig. 2.

3.2 HD48265

HD48265 is classed in the *Hipparcos* catalogue as a G5IV/V star, however we find a ΔM_V of 1.9, therefore this star is a subgiant. Again, it is extremely metal-rich, towards the top end of the metallicity scale, since its [Fe/H] is found to be +0.4 dex. A planetary companion to this star was previously published in Minniti et al. (2009) and an update to the planet's orbital parameters was published in Jenkins et al. (2009). Here, we report our latest orbital solution for this system, including more HARPS velocities and with the addition of CORALIE and MIKE data.

We found a signal with a period of 780 d and with a semi-amplitude of 28 m s^{-1} (Fig. 3) in the radial velocities of HD48265. The log-Bayesian evidence for this signal is 103.1, well above the significance threshold. Although there is a trough in the MMSE close to this period when compared to the surrounding parameter space, it is significantly lower than the noise floor at shorter periods, in particular around a period of 20 d (deepest trough), therefore the MMSE periodogram cannot be used to confirm the existence of

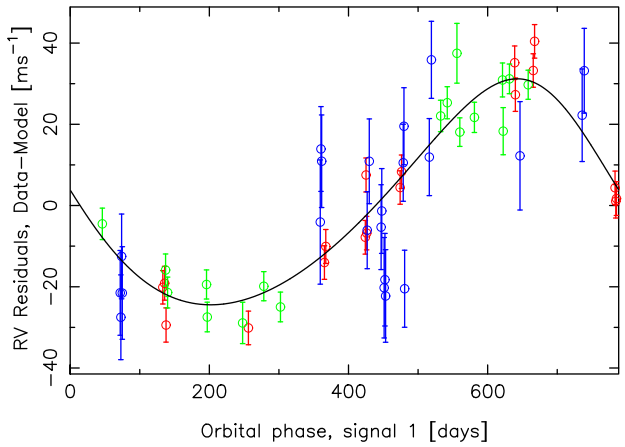

Figure 3. Phase folded CORALIE (blue), HARPS (red), and MIKE (green) velocities for the long-period signal detected in the HD48265 velocities. The solid curve represents the best-fitting Keplerian model to the data.

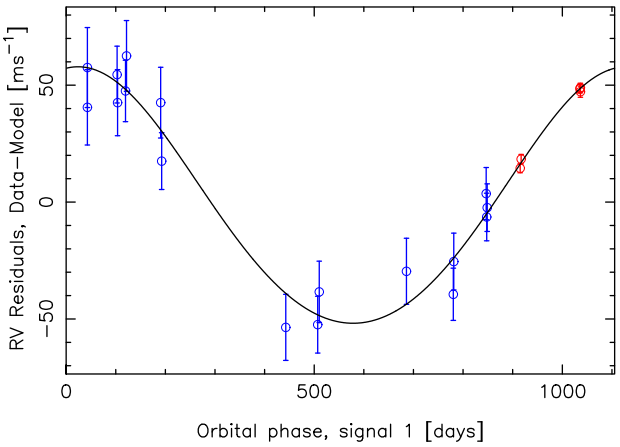

Figure 4. Phase folded CORALIE (blue) and HARPS (red) velocities for HD68402. The solid curve is the best-fitting Keplerian model.

this signal. We studied this 20 d trough to look for evidence of a signal here but nothing was clear. In fact, this trough was found to be dependent on the noise properties of the data since when the jitter parameter was considered in the periodogram analysis the evidence pointed towards a period of ∼40 d, close to twice the period, indicating it is an artefact of the interference pattern from the window function beating with the real signal in the data.

The evolved nature of the star ensures that it is an inactive and slowly rotating star and hence it is unlikely that stellar activity is the source of these signals. The minimum mass of the planet is found to be 1.47 M_J and a non-zero eccentricity was found for the signal. We note that a significant linear trend was also found that possibly indicates more companions that await discovery in this system, particularly at longer orbital periods. The method also indicated that a shorter period signal may be present, with a period close to 60 d, yet the current data does not allow us to confirm this as a genuine second planet since the signal disappears when we introduce the linear activity correlation parameters in the analysis. Also, this signal could be an alias of the detected planetary signal.

The planetary parameters we find here are generally in good agreement with those published in Minniti et al. (2009) and Jenkins et al. (2009), however the period we quote is significantly larger than that found by Jenkins et al. by ∼80 d. The differences in the periods are attributed to the lower number of high-precision HARPS data in that work, which was causing the fitting algorithm to weigh heavily towards those data points, even though they were much fewer compared to the MIKE data. This had the effect of significantly increasing the precision of the fit compared to Minniti et al., but in the presence of a linear trend, it also skewed the orbital period to lower values. All other parameters are in excellent agreement within the uncertainties.

3.3 HD68402

The star HD68402 is classed as G5IV/V, though since we find a ΔM_V of around 0.1 mag, we believe the star to be a dwarf. The metallicity of HD68402 is found to be +0.29 dex. A signal with a semi-amplitude of over 50 m s^{-1} was found at a period (∼1100 d) similar to that in the HD9174 data. The MMSE shows two long-period troughs for this data, with the detected signal found to be the second trough behind a slightly stronger trough close to 3000 d. The signal was found to have an eccentricity of 0.03, but to within the limits it can be considered as circular.

Given the mass of HD68402 is 1.12 $M_\odot$, we compute a minimum mass of just over 3 M_J for the planet. The phase folded velocities for the planetary signal are shown in Fig. 4. Since the log-Bayesian evidence is 49.4, strongly confirming the existence of a signal, and it was also found in the MMSE analysis, and by a manual fitting approach, the solution is significantly well constrained, even though there is a small gap in the phase folded curve.

3.4 HD72892

This G5V star is located at a distance of 73 pc from the Sun and has a metallicity of +0.25 dex. The star is also very inactive ($\log R'_{\rm HK}$ = −5.02) and a slow rotator ($v\sin i$ = 2.5 km s^{-1}) representing an excellent target to search for planets. We have detected a signal with a period of nearly 40 d and semi-amplitude of 320 m s^{-1}. The signal has a log Bayesian evidence value of 903.0, confirming the signal at very high significance. Given the S/N ratio between the signal amplitude and the HARPS and CORALIE uncertainties, we fully expected a large evidence ratio to confirm the nature of the signal. The signal is also clearly apparent in the MMSE periodogram as the strongest trough, adding to its reality.

We find a mass for the star of 1.02 $M_\odot$, leading to a planetary minimum mass of 5.5 M_J. This super-Jupiter also has appreciable eccentricity, at the level of 0.4, and the final Keplerian model to the phase folded velocities are shown in Fig. 5. We note that the solution gives rise to a transit probability for this star of 1.6 per cent, a relatively high likelihood of transit for such a planet–star separation.

3.5 HD128356

Using our Bayesian approach, we detected a signal with a semi-amplitude of 37 m s^{-1} and period approaching 300 d (Fig. 6) that had a log-Bayesian evidence ratio of 144.5. HD128356 is the coolest star we have included in the CHEPS sample and is classed as a main-sequence star by *Hipparcos* (K3V). We find the star to have an [Fe/H] of almost +0.2 dex, and with a ΔM_V of 0.55, it may be a subgiant star, or at least in the process of evolving on to the subgiant branch.

The star is found to be a very slow rotator, having a $v\sin i$ of only 1.3 ± 0.2 km s^{-1}, and with a low chromospheric activity of $\log R'_{\rm HK}$ of −4.8. We note that this activity level is significantly

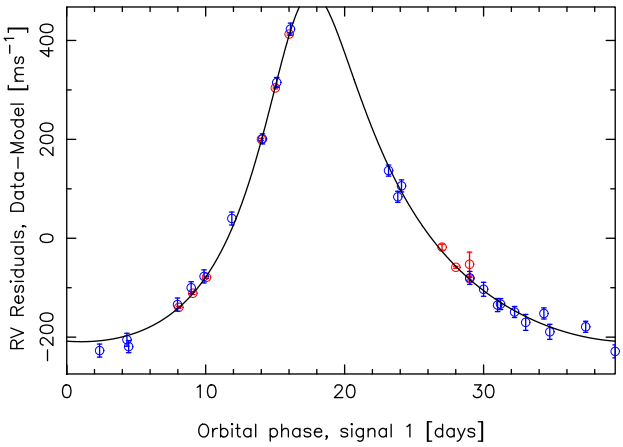

Figure 5. Phase folded CORALIE (blue) and HARPS (red) velocities for HD72892. The solid curve is the best-fitting Keplerian model.

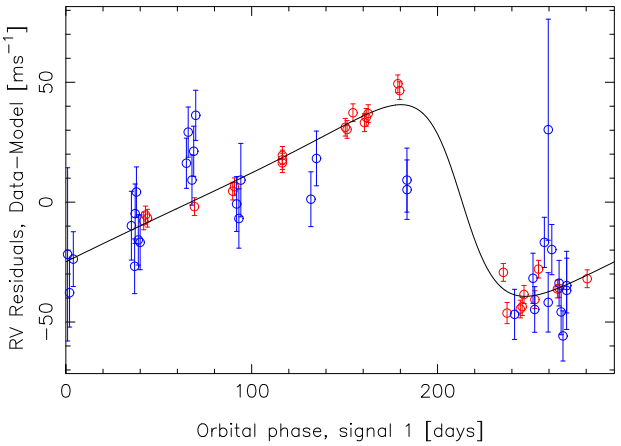

Figure 6. Phase folded CORALIE (blue) and HARPS (red) velocities for HD128356. The solid curve is the best-fitting Keplerian model.

lower than the one reported in Jenkins et al. (2011b), due to an updated $B - V$ colour used here. The colour used in Jenkins et al. was drawn from the *Hipparcos* catalogue ($B - V = 0.685$), yet the Tycho-2 catalogue magnitudes (Høg et al. 2000) give a colour >1, agreeing with what is expected for a mid-K star. Even if the star was moderately active, we would still expect the jitter to be low since mid-K type stars are not as *Doppler-noisy* as earlier type stars for a given activity level (e.g. Isaacson & Fischer 2010). This, combined with the very slow rotation of the star, indicates that it is likely a signal with a peak-to-peak amplitude of nearly 80 m s^{-1} is not caused by modulated activity effects, especially with a period close to 300 d and eccentricity of 0.8.

The signal detected in our MCMC analysis is also clearly apparent in the MMSE, being the deepest trough, despite the high eccentricity. However, an additional trough at a much longer period is also approaching a similar level of significance. There is also no apparent correlations with the activity indicators, as discussed in the next section, nor are there any detected periods in the activity measurements. Given the multimethod signal detection and lack of activity correlations, we can confidently conclude that the signal we detected has a Doppler origin, and since the mass of HD128356 was found to be around 0.65 $M_\odot$, the measured minimum mass for the planet is 0.9 M_J.

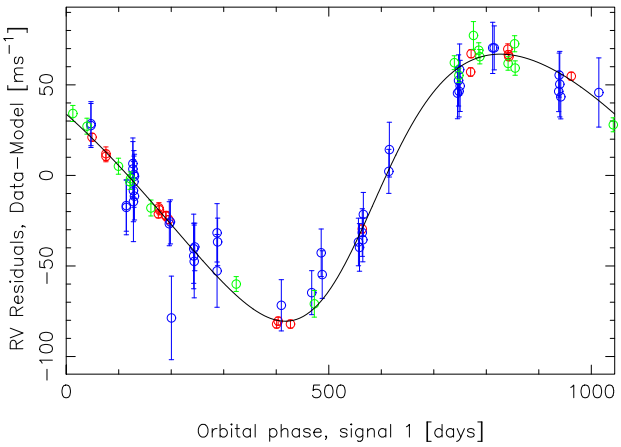

Figure 7. Phase folded CORALIE (blue), HARPS (red), and MIKE (green) velocities for HD143361. The solid curve is the best-fitting Keplerian model.

3.6 HD143361

The star HD143361 was previously shown to have a planet with a period of 1057 d (Jenkins et al. 2009; Minniti et al. 2009) and we have been conducting further reconnaissance to search for additional companions and to better constrain the orbital characteristics of the previously detected planet. The host star is a chromospherically quiet ($\log R'_{HK} = -5.12$ dex) and metal-rich ([Fe/H] = +0.22 dex) G6V star, located at a distance of 66 pc.

Our Bayesian search found a signal with a period of 1046 d with a Bayesian evidence of 491.9, relating to a planet orbiting the star with a minimum mass of 3.5 M_J (Fig. 7). From the MMSE periodogram, the signal is clearly detected, being one of the most significant periodogram detection's in our sample. The final parameters are in good agreement with those published in Minniti et al. and Jenkins et al. The orbital period found here is lower by 40 d (∼4 per cent) compared to that published in Minniti et al. but only lower by 11 d (∼1 per cent) to that published in Jenkins et al., and both are in agreement within the quoted uncertainties, which are a factor of 28.1 and 6.3 lower here than in those previous two works, respectively. Although in agreement within the quoted uncertainties, our semi-amplitude is higher than those published in the previous two works, by 9.1 and 7.1 m s^{-1}, respectively. No strong evidence for a second companion was found in this system with the current data set.

3.7 HD147873

The star HD147873 is the earliest type star in this sample of planet-hosts and is reported as a G1V star in the *Hipparcos* catalogue. Given its distance of 105 pc, the star is a little brighter than 8 mag in V. The star also appears to have a solar metallicity ([Fe/H] = −0.03 dex), is extremely inactive ($\log R'_{HK} = -5.27$ dex), and rotates at the level of nearly 6 km s^{-1}. We find a Y2 evolutionary track mass for HD147873 of 1.38 $M_\odot$.

The Bayesian search for signals in the Doppler data for this star detected two strong periodic signals with semi-amplitudes of 170 and 50 m s^{-1} for HD147873 b and c, respectively. The periods of the signals were found to be at 117 d for the stronger signal and 492 d for the weaker of the two signals. The log-Bayesian evidences we found for these signals were 1131.5 and 145.2. The MMSE periodogram also detected both these signals rather easily; the second becoming detectable in the residuals of the data once the first signal was removed, as shown in Appendix B1. We find

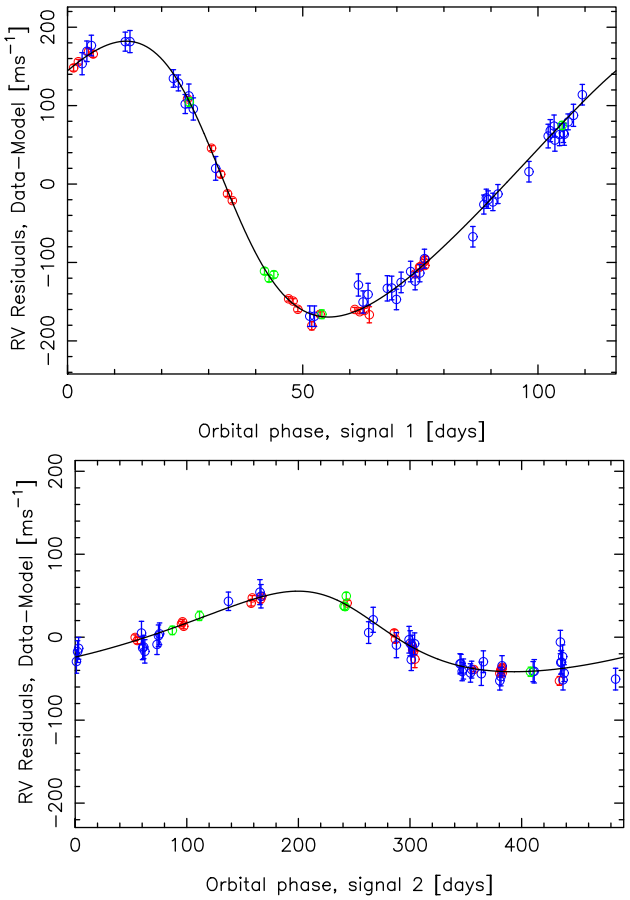

Figure 8. Phase folded CORALIE (blue), HARPS (red), and MIKE (green) velocities for HD147873 for the short (upper panel) and long (lower panel) period signals. The solid curves represent the best-fitting Keplerian models to the data.

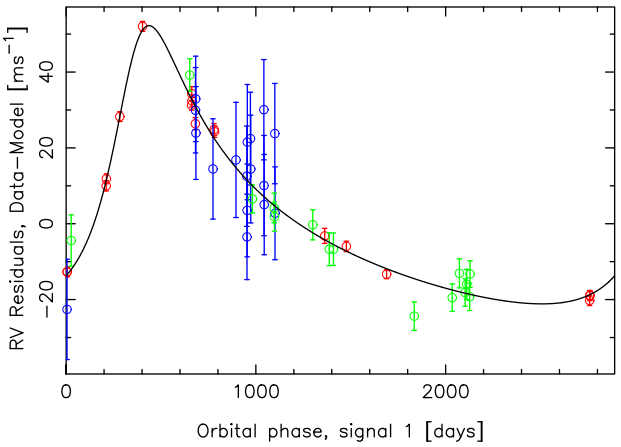

Figure 9. Phase folded CORALIE (blue), HARPS (red), and MIKE (green) velocities for HD152079. The solid curve is the best-fitting Keplerian model.

planetary minimum masses of 5.1 and 2.3 M_J for the short and longer period planets, respectively. Both Keplerian fits to the data are shown in the upper and middle plots in Fig. 8. The inner planet is also only one of two in this sample that has a transit probability of over 2 per cent, a value that encourages the search for transits from intermediate period planets.

Given, we have discovered two giant planets with a semimajor axis difference of only 0.84 au between them, we decided to test if the system architecture was dynamically stable. We ran Gragg–Burlich–Stoer integrations in the SYSTEMIC CONSOLE (Meschiari et al. 2009) over a period of 10 Myr to study the evolution of the orbits of both planets. We find the eccentricity of the orbits librate with a period of around 12 000 yr but the system itself remains dynamically stable across this timespan. Systems with multiple giant planets are interesting laboratories for dynamical studies and this system may warrant further detailed dynamical study, especially if more massive companions are discovered with the addition of more data.

3.8 HD152079

HD152079 is classed as a G6 main-sequence star in the *Hipparcos* catalogue and our previous work found it to be inactive ($\log R'_{\rm HK}$ = −4.99 dex) and metal-rich (+0.16 dex in [Fe/H]), which may explain the 0.5 mag ΔM_V. We found the mass of the star to be 1.1 $M_\odot$. This is also one of the stars in this sample with a previously announced planet candidate detected in orbit (Arriagada et al. 2010).

A signal with a period of 2900 d and semi-amplitude of 31 m s^{-1} was detected in the Doppler data of HD152079. The log-Bayesian evidence ratio was found to be 99.1, highly significant, and the signal was found to have an eccentricity over 0.5. It is likely for this data set that the moderate eccentricity of the signal is hampering its detection in the MMSE periodogram. In addition, there is a presence of a linear trend in the data that indicates there is a long-period secondary companion to this star, and since linear trends are not considered in the MMSE model, the interference here could also be confusing the algorithm. Yet there is a fairly strong trough showing at a period of ∼1400 d, which is close to half the Bayesian detected signal, and could be related to the Doppler signal, or an additional companion that is at a 2:1 resonance site, which could also explain the eccentric shape of the one planet signal (Marcy et al. 2001; Anglada-Escudé, López-Morales & Chambers 2010). In any case, we found the minimum mass of HD152079*b* to be 2.2 M_J and the Keplerian model fit is shown in Fig. 9. These values are in good agreement with those presented in Arriagada et al., except the precision quoted here is much higher. For instance, the period of 2097 ± 930 d quoted in their work has been constrained to 2899 ± 52 d here, a factor of 18 increase in precision and pushing the planet's orbit upwards by nearly 900 d. This precision increase is also mirrored directly in the semi-amplitude precision, lowering it from 58 ± 18 m s^{-1} to 31.3 ± 1.1 m s^{-1}.

3.9 HD154672

This star has a *Hipparcos* classification of G3IV, confirmed by our measurement of 0.94 mag from the main sequence. Part of the elevation from the main sequence can also be explained by the metallicity enrichment of 0.11 dex. The star is also a slow rotator, having a $v\sin i$ of 2.2 km s^{-1} and was found to be very chromospherically inactive ($\log R'_{\rm HK} = -5.12$ dex). The position on the HR-diagram gives rise to a mass of 1.08 $M_\odot$.

A signal with a period of 164 d and semi-amplitude of 176 m s^{-1} was found in the Doppler timeseries of HD154672, with a log-Bayesian evidence ratio of 1709.2, the most significant signal in this data set. The signal is also clearly apparent in the MMSE periodogram, the period though being significantly stronger than any other periods across the parameter space. The eccentricity of the signal was found to be 0.6, giving rise to a planet with a minimum

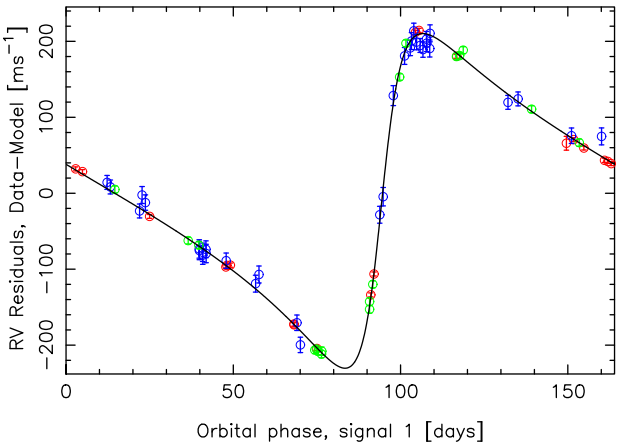

Figure 10. Phase folded CORALIE (blue), HARPS (red), and MIKE (green) velocities for HD154672. The solid curve is the best-fitting Keplerian model.

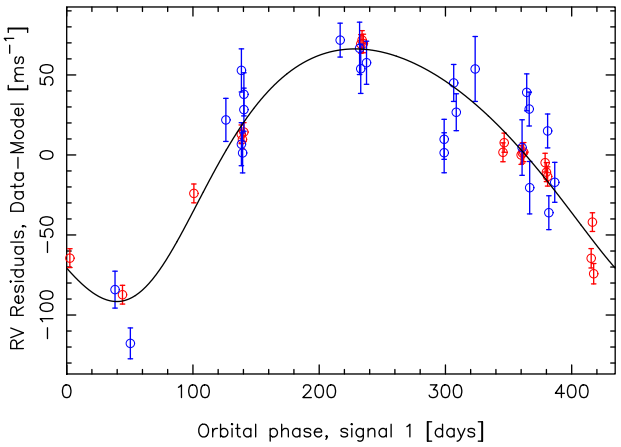

Figure 11. Phase folded CORALIE (blue) and HARPS (red) velocities for HD165155. The solid curve is the best-fitting Keplerian model.

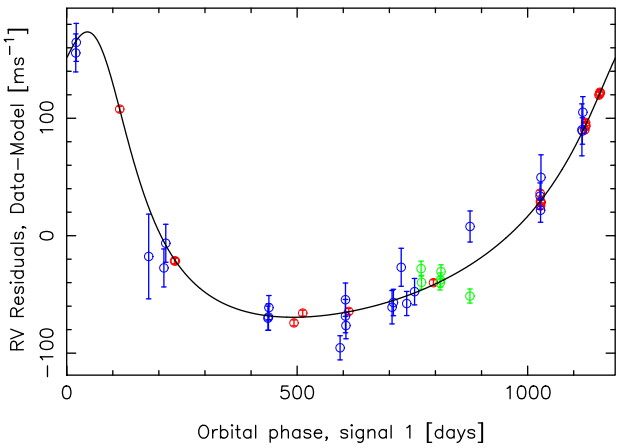

Figure 12. Phase folded CORALIE (blue), HARPS (red), and MIKE (green) velocities for HD224538. The solid curve is the best-fitting Keplerian model.

mass of nearly 5 M_J. The values we find are in good agreement with the values previously published for this planet in López-Morales et al. (2008), with the period agreeing to within 1 h and the minimum mass being slightly lower here by only 0.23 M_J, but well within the 1σ uncertainties. Given the inclusion of higher quality data in this analysis, we find the jitter for this star to be 2 m s^{-1}, a factor 2 lower than that quoted in Lopez-Morales et al., demonstrating that a significant fraction of their jitter was instrumental noise. The model fit is shown in Fig. 10.

Our search for additional planets in the combined data sets did not yield any positive results, therefore no firm evidence exists for any additional companions in this system. If the eccentricity from this planet is genuine and not due to the superposition of mixed signals from other giant planets in resonant orbits (see Anglada-Escudé et al. 2010; Wittenmyer et al. 2012), then the transit probability for this object is found to be the highest in the current sample of intermediate and long-period planets, at 2.5 per cent.

3.10 HD165155

The *Hipparcos* catalogue classifies HD165155 as a G8 main-sequence star, however with a elevation above the main sequence of 1.4, this star can be considered as a subgiant. The star is located at a distance of 65 pc, and from spectroscopy we have found a $\log R'_{\rm HK}$ activity index of −5.18 dex, a rotational velocity of 1.5 km s^{-1}, and an [Fe/H] metallicity index of 0.09 dex. Comparison to Y2 evolutionary models yield a mass for the star of 1.02 $M_\odot$.

A signal has been detected in the RV data for HD165155 with a period of 435 d and a semi-amplitude of 76 m s^{-1}. The log-Bayesian evidence for the signal was found to be 168.9, securely above the significance threshold. The eccentricity was found to be 0.20 and therefore the final minimum mass of the companion is calculated as 2.9 M_J (Fig. 11). A two-planet model search produced statistically significant evidence for a second signal in the data; however given the limited number of measurements, we could not confirm a unique secondary signal at this time. No statistically significant troughs were detected in the MMSE periodogram for this star, which may be due to the presence of a secondary signal that is interfering with the primary signal. Indeed, the inclusion of a strong linear trend was necessary to constrain this signal, and since linear trends are not included in the MMSE modelling approach, this trend is likely the reason why the MMSE approach failed to detect this signal.

3.11 HD224538

The main *Hipparcos* catalogue lists HD224538 as an F9 dwarf or subgiant located at a distance of 78 pc. With a calculated ΔM_V of 0.63 and a high overabundance of metals in the star ([Fe/H] = +0.27 dex), the possibility remains that this star is either on the main sequence or crossing into the subgiant branch. The star is both a slow rotator ($v \sin i = 3.9$ km s^{-1}) and chromospherically inactive ($\log R'_{\rm HK} = -4.99$ dex). From comparisons to Y2 isomass tracks on a HR-diagram, we found a mass of 1.34 $M_\odot$ for HD224538.

Our Bayesian algorithm found a signal with a period of 1189 d, a semi-amplitude of 107 m s^{-1}, and an eccentricity of 0.46, shown in Fig. 12. The log-Bayesian evidence ratio for the signal was found to be highly significant at 391.0. The MMSE periodogram also clearly detected this signal. Therefore, a planet with a minimum mass of 6.0 M_J is found to be orbiting this star. This is reminiscent of the gas giant planet 14 Her *b* that has a broadly similar mass, period, and eccentricity (Butler et al. 2003) and such planets appear to be rare. Even though 14 Her is an early K-dwarf star, it does have a supersolar metallicity (+0.43 ± 0.08 dex) similar to HD224538, likely necessary to form such high-mass planets. No additional

Table 2. Orbital mechanics for all planetary systems described in this work.

Parameter	HD9174*b*	HD48265*b*	HD68402*b*	HD72892*b*	HD128356*b*	HD143361*b*
Orbital period P (d)	1179 ± 34	780.3 ± 4.6	1103 ± 33	39.475 ± 0.004	298.2 ± 1.6	1046.2 ± 3.2
Velocity amplitude K (m s^{-1})	20.8 ± 2.2	27.7 ± 1.2	54.7 ± 5.3	318.4 ± 4.5	36.9 ± 1.2	72.1 ± 1.0
Eccentricity e	0.12 ± 0.05	0.08 ± 0.05	0.03 ± 0.06	0.423 ± 0.006	0.57 ± 0.08	0.193 ± 0.015
ω (rad)	1.78 ± 0.66	6.0 ± 2.4	0.3 ± 2.3	6.010 ± 0.014	1.47 ± 0.08	4.21 ± 0.06
M_0 (rad)	3.5 ± 1.3	4.9 ± 1.4	6.0 ± 2.2	2.714 ± 0.010	3.1 ± 0.7	3.21 ± 0.14
$m\sin i (M_J)$	1.11 ± 0.14	1.47 ± 0.12	3.07 ± 0.35	5.45 ± 0.37	0.89 ± 0.07	3.48 ± 0.24
Semimajor axis a (au)	2.20 ± 0.09	1.81 ± 0.07	2.18 ± 0.09	0.228 ± 0.008	0.87 ± 0.03	1.98 ± 0.07
$\gamma_{\rm HARPS}$ (m s^{-1})	-7.2 ± 1.4	-1.5 ± 1.6	-34.2 ± 8.2	-37.8 ± 1.7	-0.1 ± 1.9	-1.2 ± 0.8
$\gamma_{\rm CORALIE}$ (m s^{-1})	-1.6 ± 3.0	-4.3 ± 2.6	-10.6 ± 4.6	48.7 ± 3.2	9.4 ± 2.7	3.4 ± 2.2
$\gamma_{\rm MIKE}$ (m s^{-1})	–	-3.5 ± 1.4	–	–	–	-26.6 ± 1.2
$\sigma_{\rm HARPS}$ (m s^{-1})	1.8 ± 0.6	6.0 ± 0.6	1.7 ± 0.9	2.2 ± 0.7	3.9 ± 0.7	2.3 ± 0.6
$\sigma_{\rm CORALIE}$ (m s^{-1})	2.2 ± 1.0	2.7 ± 1.1	2.0 ± 1.0	2.0 ± 1.0	2.1 ± 1.0	1.8 ± 0.9
$\sigma_{\rm MIKE}$ (m s^{-1})	–	2.8 ± 0.8	–	–	–	2.8 ± 0.8
$\dot{\gamma}$ [ms^{-1} yr^{-1}]	–	–	–	–	–	–
$P_{\rm T}$	0.3 per cent	0.5 per cent	0.2 per cent	1.6 per cent	0.4 per cent	0.2 per cent
$N_{\rm Obs}$	29	57	20	32	60	80
$\ln B(k, k-1)$	42.1	103.1	49.4	903.0	144.5	491.9
Parameter	HD147873*b*	HD147873*c*	HD152079*b*	HD154672*b*	HD165155*b*	HD224538*b*
Orbital period P (d)	116.596 ± 0.023	491.54 ± 0.79	2899 ± 52	163.967 ± 0.009	434.5 ± 2.1	1189.1 ± 5.1
Velocity amplitude K (m s^{-1})	171.5 ± 1.2	47.9 ± 1.7	31.3 ± 1.1	176.3 ± 0.7	75.8 ± 3.0	107.0 ± 2.4
Eccentricity e	0.207 ± 0.013	0.23 ± 0.03	0.52 ± 0.02	0.600 ± 0.004	0.20 ± 0.03	0.464 ± 0.022
ω (rad)	1.40 ± 0.05	0.73 ± 0.20	5.67 ± 0.06	4.63 ± 0.01	3.7 ± 0.2	0.40 ± 0.03
M_0 (rad)	1.65 ± 0.07	3.09 ± 0.20	0.8 ± 0.8	3.60 ± 0.02	0.9 ± 0.8	0.3 ± 0.3
$m\sin i (M_J)$	5.14 ± 0.34	2.30 ± 0.18	2.18 ± 0.17	4.73 ± 0.32	2.89 ± 0.23	5.97 ± 0.42
Semimajor axis a (au)	0.522 ± 0.018	1.36 ± 0.05	3.98 ± 0.15	0.59 ± 0.02	1.13 ± 0.04	2.28 ± 0.08
$\gamma_{\rm HARPS}$ (m s^{-1})	59.0 ± 1.2	–	-37.9 ± 7.0	5.2 ± 0.7	-59.6 ± 18.7	-15.3 ± 1.5
$\gamma_{\rm CORALIE}$ (m s^{-1})	5.4 ± 2.2	–	-44.8 ± 8.5	-44.6 ± 2.0	-87.7 ± 20.1	27.0 ± 2.7
$\gamma_{\rm MIKE}$ (m s^{-1})	37.6 ± 3.1	–	-13.6 ± 6.8	28.2 ± 1.2	–	55.9 ± 4.3
$\sigma_{\rm HARPS}$ (m s^{-1})	2.6 ± 0.7	–	1.5 ± 0.6	2.1 ± 0.5	5.8 ± 0.6	2.9 ± 0.6
$\sigma_{\rm CORALIE}$ (m s^{-1})	1.9 ± 0.9	–	2.0 ± 1.0	2.2 ± 1.0	3.7 ± 1.2	2.0 ± 1.0
$\sigma_{\rm MIKE}$ (m s^{-1})	2.4 ± 1.0	–	2.7 ± 0.8	3.6 ± 0.7	–	5.2 ± 0.7
$\dot{\gamma}$ [ms^{-1} yr^{-1}]	2.94 ± 0.68	–	1.72 ± 0.47	–	4.00 ± 1.19	–
$P_{\rm T}$	2.3 per cent	0.7 per cent	0.1 per cent	2.5 per cent	0.4 per cent	0.2 per cent
$N_{\rm Obs}$	66	–	50	72	38	50
$\ln B(k, k-1)$	1131.5	145.2	99.1	1709.2	168.9	391.0

The uncertainties on the $m\sin i$ and semimajor axis consider the uncertainties on our stellar mass estimate of 10 per cent.
The γ offset is the value after subtracting off the mean of the data set.
The σ terms parametrize the excess noise in our model fits, aka jitter.
The ln B(k,k-1) are generally the one-planet models (e.g. B(1,0)) except for HD147873 which is a two-planet model (B(2,1)).
$P_{\rm T}$ is each planet's transit probability.
$N_{\rm Obs}$ are the total number of radial velocities per target star.

statistically significant signals were found in the current data set. All model parameters for these planet candidates are shown in Table 2.

3.12 Line modulation tests

Although these stars are very inactive and slowly rotating and the Doppler signals we have detected are generally very large compared to the uncertainties (most are significantly larger than 20 m s^{-1}), it is useful to rule out line modulations that could originate from stellar activity as the source of the variations. The activity parameters employed are the Ca II HK line doublet, the bisector span (BIS), the CCF full width at half-maximum (FWHM), the Hα line, and the H I D3 line. These indices were selected since they have previously been shown to be good tracers of stellar magnetic activity, and/or spectral line modulations (e.g. Queloz et al. 2001; Santos et al. 2010; Robertson et al. 2014). In Fig. 13, we show four of the tests we have carried out to rule out these modulations as the source of the detected RV shifts for the star HD128356, originally believed to be the most active star in the sample due to the erroneous $B-V$ colour. We note that we do not show the CCF FWHM test for this star since there are large variations with a few outliers, but no correlation exists.

In the upper plot of Fig. 13, we show how the BIS values vary as a function of the RV data sets. The BIS values for HARPS were taken from the HARPS-DRS and measured following the method explained in Queloz et al. (2001). The CORALIE BIS values were calculated using a similar procedure. No significant correlation between the radial velocities and the BIS measurements are found and we highlight this by showing the best-fitting linear trend to the data. The unweighted Pearson rank correlation coefficient has a value of 0.23, signifying a weak correlation, however when the correlation is weighted by the measurement uncertainties on the RV and BIS values, the coefficient drops to 0.11, or no evidence at all for any correlation.

We also searched for a correlation between the chromospheric activity S-indices and the velocities as a second useful

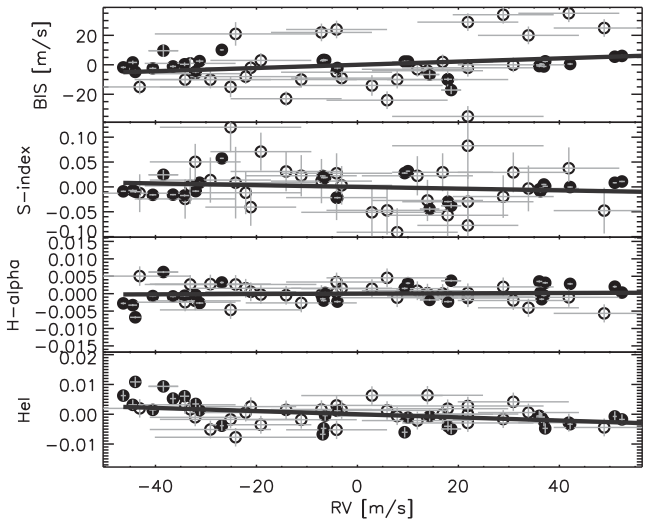

Figure 13. The four plots from top to bottom show the linear correlations between the radial velocities and the BIS velocities, the *S*-indices, the Hα indices, and the H I indices for HD128356, respectively, where CORALIE data is represented by open rings and HARPS data by filled circles. The solid lines are the best-fitting linear trends to the data.

discriminant that activity is not the source of the observed variations. The measurement of these *S*-indices for HARPS was briefly discussed in Jenkins et al. (2013b) and therefore here we only discuss the CORALIE activity measurement method in Appendix D. In any case, the method for both is similar, except for HARPS we use the extracted 1D order-merged spectrum, whereas for CORALIE spectra we perform the calculations using the extracted 2D order-per-order spectrum, similar to the method discussed in Jenkins et al. (2006).

The second plot in Fig. 13 shows these chromospheric activity *S*-indices as a function of the RV measurements and no apparent correlation is found. The best unweighted linear fit is shown by the solid line and confirms the lack of any correlation between the two parameters. The correlation coefficient also confirms this since an unweighted r coefficient of -0.09, similar to the weighted BIS, is not statistically significant, dropping even lower when considering the weights.

The lower two plots in the figure show the linear correlations against the measured Hα and H I D3 activity indicators, respectively. These indices were calculated following the methods discussed in Santos et al. (2010). For both of these indices, no significant correlation is found when combining the CORALIE and HARPS data. Some moderate correlation between the H I index and the velocities is seen, with an unweighted r correlation coefficient of -0.64 for the HARPS only measurements, decreasing to -0.39 when the CORALIE measurements are added. Judging by the lower panel in the figure, no striking correlation is apparent, given what would be expected for this level of correlation, and once the measurement uncertainties are included to weight the correlation coefficient, the value drops significantly to be in agreement with zero correlation. In fact, we can see that the majority of the data are uncorrelated, from radial velocities between -25 and $+55$ m s^{-1}, with only a few offset data points clustered around -40 m s^{-1}driving the correlation.

As an aside, if we apply the relationships in Saar & Donahue (1997) and Hatzes (2002) to calculate the spot coverage expected for a star with the rotational period of HD128356, in order to produce an RV amplitude in agreement with that observed here, then $\sim$5 per cent of disc spot coverage is required, which would likely exhibit as photometric variations that are not observed (see below).

Although the activity indicators for the other stars reported in this work show no evidence for any strong linear correlations, measured by the Pearson Rank correlation coefficient, against the radial velocities, we report the moderately correlated data sets ($|0.5| \geq r \geq |0.75|$). For HD48265, the HARPS BIS values correlate with the radial velocities with an r value of 0.59 ± 0.25, indicating some moderate correlation between the two parameters. We also note that both the Hα and H I indices have values of 0.47 and -0.41, respectively, yet there are large parts of parameter space that are undersampled by including only the HARPS data alone. When adding in the CORALIE measurements, we find these values decrease to 0.22, 0.12, and -0.33 for the three quantities, respectively, with uncertainties of ± 0.16, indicating that these correlations are not the source of the velocity signal for this star.

The star HD68402 shows HARPS velocity correlations with the BIS and H I indices with r values of 0.79 and 0.52, respectively. We note that there are only five HARPS data points for this star so no result here can be deemed significant. Furthermore, once the CORALIE values are included we find values of 0.01 and 0.12 for these parameters, respectively. When including the CORALIE measurements, we find a moderate correlation appears between the velocities and the CCF FWHM measurements ($r = 0.52 \pm 0.23$). Again, there appears no significant correlations in the analysis.

Another star with a limited number of HARPS spectra (eight measurements) that give rise to an apparent moderate correlation between the radial velocities and activity indicators is HD72892. The HARPS CCF FWHM and H I measurements have Pearson rank correlation coefficients of 0.58 and 0.73, respectively, with uncertainties of $\pm$ 0.38. When the CORALIE measurements are added to the HARPS data, we find this correlation becomes insignificant, with values of only -0.47 and 0.10, respectively, and uncertainties of $\pm$ 0.19. However, the Hα indices now exhibit a moderate correlation with the velocities ($r = 0.57$). The signal for this star has an amplitude of nearly 320 m s^{-1} and a period of $\sim$40 d. Although 40 d is a plausible rotational period for this type of very inactive G5 dwarf star, the fact that it is so inactive indicates that such a large signal would be difficult to produce through spot rotation. In fact, if we calculate the spot coverage as above, then 20–25 per cent of disc spot coverage is required, which can be ruled out based on the photometric stability and the low $\log R'_{\rm HK}$ measurement.

For HD152079, the HARPS Hα index correlates with the velocities with a correlation coefficient r of 0.66 ± 0.24, although none of the other indicators show any evidence for correlations, and when adding the CORALIE data, the correlation coefficient decreases to a value of only 0.47 ± 0.17. We note that the variations in the measurements are only changing at the few $\times 10^{-3}$ level, from 0.203 to 0.208 in our HARPS Hα index.

The star HD165155 shows a correlation between the velocities and the HARPS CCF FWHM with a value of -0.66 ± 0.23, although with a large spread. Addition of the CORALIE CCF FWHM decreases the value to 0.12 ± 0.17, rendering this result insignificant.

HD224538 shows moderate correlation between the velocities and the Hα indices at the level of 0.69 ± 0.22 in the HARPS data, and at the level of 0.27 ± 0.15 when the CORALIE values are included. Again, the variation is only at the few $\times 10^{-3}$ level, which is likely to be insignificant.

The periodogram analysis for each of the five activity indicators did not reveal any significant periods that could explain the detected signals in any of the stars considered here (see Appendix E1),

however a few features do appear. For the star HD72892, there are emerging peaks in the periodograms of the BIS, FWHM, S and H I indices at periods between 11 and 13 d, and although this region is distinct from the detected planetary signal, these may be linked to the rotational period of the star; however, there is a peak in the window function at 22.5 d that could be giving rise to a peak at the first harmonic in these indices. For HD128356, the moderately active star, both the BIS and FWHM timeseries show peaks that agree with a period around 1250 d that has no counterpart in the window function, meaning this could be a magnetic cycle, but it is far from the detected Doppler signal period. HD147873 does show a unique peak close to the lower period signal in the radial velocities in the H I indices with a period of around 120 d, yet the peak is not significant. The Hα indices show an emerging peak with a period of ∼70 d as the strongest signal for HD165155 that could point to the rotation period for this star but there is a window function peak emerging at 63.5 d, that is likely unrelated to this peak, but is worthy of note. In any case, neither of these are related to the detected Doppler signal in the radial velocities. Finally, the star HD224538 shows evidence for two peaks in the periodograms of the BIS and Hα indices that are in good agreement with signals with periods of 20 d, which again could be a good candidate for the rotational period for this star; however, the fifth strongest peak in the window function is found to be at 19 d, meaning there is a non-insignificant probability that this peak is being boosted by the sampling.

3.13 Photometric analysis

We decided to photometrically search for a secure rotational period for these stars by employing frequency analyses of the V-band All Sky Automated Survey (ASAS; Pojmanski 1997) photometric data. We have previously shown that such analyses can shed light on the rotational periods of planet-host stars and/or short-period and long-period magnetic cycles (e.g. Anglada-Escudé et al. 2013; Jenkins & Tuomi 2014). We tend to focus on the best-quality data, ASAS grade A or B using the smallest ASAS apertures that are best for point sources, and typical baselines cover ∼9 yr at a sampling cadence of ∼3 d. Out of all the 11 planet-hosts considered in this work, six show evidence for a significant rotational period or long-period magnetic cycle in the photometry, and these are summarized below, with particular focus paid to HD165155.

The six stars showing evidence for a photometric signal in the ASAS timeseries are HD68402, HD147873, HD152079, HD154672, HD165155, and HD224538, and the Lomb–Scargle periodograms for these six stars are shown in Appendix F1. We do not show the periodograms for the remaining six stars since they exhibit no significant frequency peaks. The periodogram for HD68402 shows two strong peaks emerging at periods of 312 and 2000 d. Neither of these signals reside at periods close to the detected Doppler signal in the radial velocities, however their strength suggests there may be some long-term magnetic cycle at play within this star.

The stars HD147873, HD152079, HD154672, and HD224538 all show evidence for long-period modulated spot activity, with periods at the extremities of the data timeseries and periodogram sampling ∼5000–10 000 d. These could be real long-term spot cycles or they could be sampling features due to the limited baselines of the data sets. However, none of these features appear to coincide with the detected RV signal periods, or harmonics there-of. HD154672 has a velocity signal detected at just over 160 d, far from any long-period magnetic cycle, whereas the signal in the HD224538 velocities has a period of a few thousand days, which could agree with any potential photometric signal in the ASAS data that is not due to the limited data baseline. However, our analysis never indicated that any correlations were evident between the radial velocities and the activity indicators for this star, and its inactive nature, along with the strength of the RV signal ($K = 110$ m s^{-1}), which would make an activity origin unlikely for a star of this type. The evidence from these analyses points to the origin of the detected signals as being due the gravitational influence of orbiting planets.

The star HD152079 has a detected signal in the velocities with a period of a few thousand days, which is approaching the regime where a long-period magnetic cycle could be present due to the ASAS photometric periodogram, yet the amplitude of this signal is a little over 30 m s^{-1} for this very inactive star. The structure of the long-period signals in the power spectrum of these stars are very similar, which argues that the frequencies emerge due to the sampling baseline. A further secondary peak exists in the photometric periodogram for this star at ∼830 d. Since this is too short to be associated with the signal in the radial velocities, it is not the origin of that signal but could be a possible sampled magnetic cycle. In any case, the nature of the RV signal is likely Doppler and from an orbiting planetary mass candidate.

We note that for HD147873 and HD224538, additional peaks arise in the periodograms at periods that could be in the range of rotational periods for stars with these types of rotational velocities and stellar radii, or could relate to additional magnetic cycles. For HD147873, there is a strong peak at a period of 29.5 d, very close to the lunar cycle, and since this period was found to arise in other ASAS timeseries, it is likely this is a sampling alias and not the star's rotational period. For HD224538, the next strongest peak is located at 385 d, with again the 29.5 d period being detected. The 385 d peak is within a small cluster of peaks that surround the Earth's orbital period, therefore it is likely that this is another sampling alias. Hence, it is unlikely that we have made a significant detection of the rotational period for any of these stars, with only tentative detections of long-period magnetic cycles.

Finally, we discuss the photometric analysis for the star HD165155 independently, since there is an indication of a peak in the periodogram that is close to the period of the detected signal in the RV measurements. Given that the signal is rather strong, it is unlikely that activity is the source of the signal at this type of period. We also note that the orbital separation is too large to produce star–planet interactions that could cause any photometric signal. From the ASAS periodogram in Appendix F1, we can see that again a long-period signal emerges, but after this signal, there are two fairly strong peaks with periods of 454 and 344 d. The 454 d signal is the second strongest after the long-period peak and it closely matches the period of the signal in the radial velocities at 452 d, indicating the signal could arise from activity or pulsations. As mentioned above, no similar periodicities were found in the activity indicators and since the *Hipparcos* photometry for this star only consists of 67 measurements, with a scatter in the data of 0.019 mag, no significant periodicity was found in this data either. We also note that by removing the long-period trend with periods of 10 000 d or more removes the signal at 454 d, signifying it is linked to this long-period trend and therefore likely not a true magnetic cycle that could induce such an RV signal as we observe.

There exists a small possibility that the detected RV signal is not of Doppler origin and is due to line asymmetries from stellar activity on this subgiant star, even though the existence of this photometric period is difficult to causally connect to the origin of the RV signal without corroborating periodicities in the spectral activity indicators. Without garnering more data, and since the

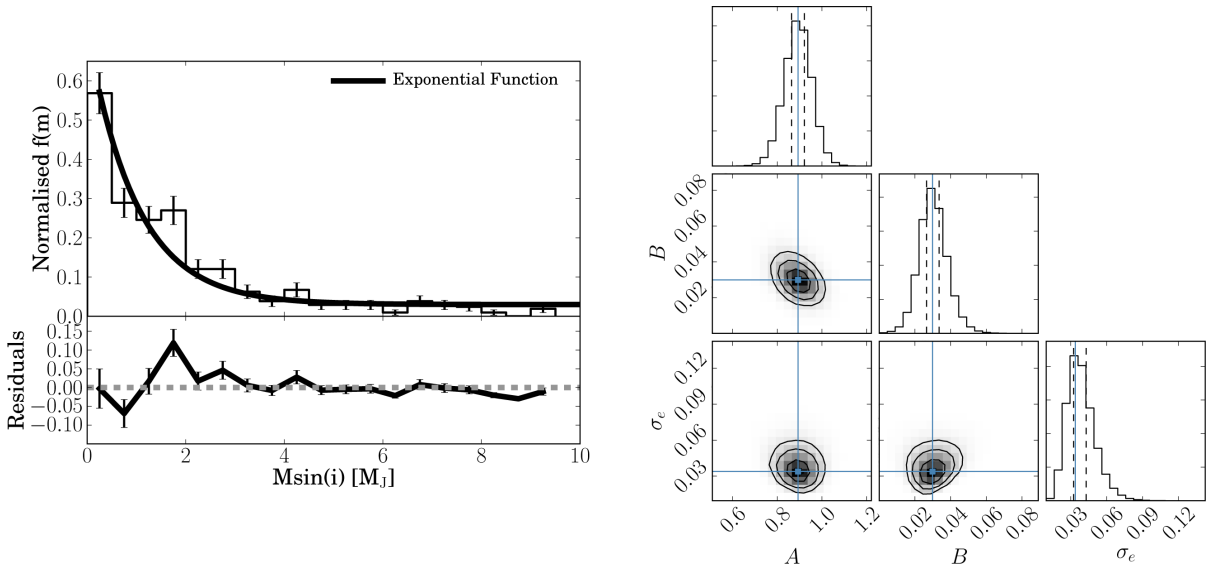

Figure 14. Normalized mass function distribution showing an exponential fit to the data for 444 exoplanet candidates (left). The associated uncertainties have been calculated assuming Poisson statistics. The right plot shows the parameter space contours and histograms (aka. a corner plot; Foreman-Mackey 2016, corner.py: corner.py v1.0.2. Zenodo. 10.5281/zenodo.45906) constructed from the MCMC chains. The contours show the exponential scaling (A), the exponent (α), and the excess noise for 1σ, 2σ, and 3σ percentiles radiating outwards from the point of maximum probability of the distributions. The cross-hairs mark the values determined from the maximum likelihood best fit. The right-edge plots show the histogrammed distributions collapsed in only the x dimension, where the mean (solid) and 1σ (dashed) ranges are highlighted.

detected photometric peak in the periodogram could be an alias that is associated with a longer period signal or the window function of the data, we still consider the RV signal as due to an orbiting companion. If, on the other hand, the signal in the velocities is genuinely of astrophysical origin, this data set would serve as a warning when trying to understand the origin of signals in RV timeseries of subgiant stars, even when the signal amplitude is relatively large, and there are no correlations or periodicities in the spectral activity indicators. Thorough searches of existing photometric data should always be performed, where possible, to help to confirm the reality of proposed planetary systems.

4 PLANET POPULATION DISTRIBUTIONS

The high-metallicity selection bias in our programme means we are generally targeting gas giant planets. The working hypothesis being that if such planets are formed through core accretion processes, then large cores can form quickly due to the enrichment of the protoplanetary disc, which gives the planetesimals sufficient time to accrete gaseous material to reach large masses after they cross the critical core mass limit of around 10 $M_\oplus$ (Mizuno 1980).

4.1 Mass function

The observed mass distribution is a key observational constraint for planet formation models, a constraint which has previously been fit by smooth power-law trends with indices around -1 (e.g. Butler et al. 2006; Lopez & Jenkins 2012). In Fig. 14, we show the results of applying an exponential function to the data, which we found to be more suited to the current distribution of exoplanets that have been detected over a wide range in stellar mass,

$$f(m) = A \times e^{\mathrm{msin}(i)} + B, \quad (2)$$

where $f(m)$ is the model function that we fit to the data and A and B are the scaling parameter and offset of the model that are left as free parameters to be found following a maximum likelihood procedure with the following Gaussian likelihood function:

$$\mathcal{L}(\Theta) = -0.5 \times \log(2\pi) - \sum_i \log(\sigma_{t,i}) - \frac{\sum_i (y_i - f(m)_i)^2}{\sigma_{t,i}^2} \quad (3)$$

$$\sigma_{\mathrm{t},i} = \sqrt{\sigma_{\mathrm{p},i}^2 + \sigma_{\mathrm{e},i}^2}. \quad (4)$$

Here, $\mathcal{L}$ is the likelihood function for parameters Θ, y is the observed data (mass function histogram points) for all i histogram points, and σ_p and σ_e are the Poisson uncertainties and any excess uncertainty for each of the values, respectively. This procedure finds the following values for the modelled parameters 0.89 ± 0.03, $0.030^{+0.004}_{-0.003}$, and $0.034^{+0.009}_{-0.002}$ for A, B, and σ_e, respectively. The uncertainties on these parameters were determined using an MCMC procedure in PYTHON, employing the EMCEEnumerical package (Foreman-Mackey et al. 2013). We used 100 walkers and ran chains of 10 000 steps in length, with a 1000 step burn-in, which relates to a final chain length of 900 000 steps, with a final mean acceptance rate of 49 per cent. The parameter values we measure are insensitive to small changes in the bin size used in the histogram, which we set to be 0.5 M_J, a value that allows enough samples in most of the bins to reflect the smoothly varying distribution.

At the right of Fig. 14, we show the parameter extent probed by the chains, where we used uniform priors for the parameters except the excess uncertainty, where we employed a Jeffries prior where the probability is proportional to $1/\sigma$. The distribution of the parameters are well confined to the region around the maximum likelihood value for each, showing that the model we put forward is an acceptable representation of the current exoplanet mass function. We note that the A and B parameters follow Gaussian distributions, whereas the excess noise parameter is more like a skewed Gaussian or Poisson distribution, where the lower 1σ credibility limit is found to be close to the maximum likelihood value of 0.03. In any case, it seems that the mass function appears to be fairly well described by an exponential function.

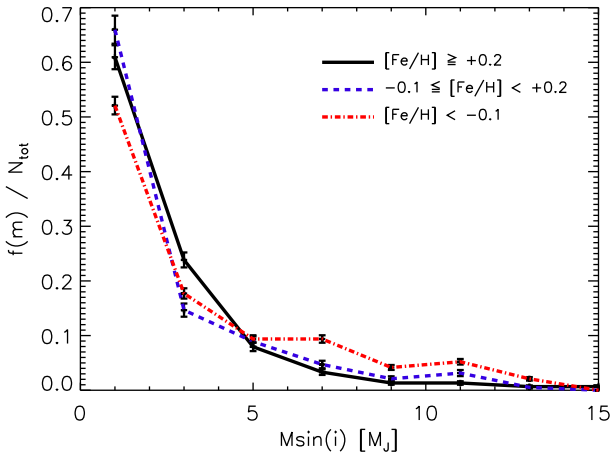

Figure 15. The observed mass distribution split into three bins with different metallicity distributions and a binsize of 2 M_J. The solid black curve is for the most metal-rich planet-hosts, the dashed blue curve is for the intermediate metallicity stars, and the dot–dashed red curve is the distribution for all metal-poor stars. The metallicity cuts are shown in the key.

4.2 Mass–metallicity functions

As Fig. 15 shows, we tested if there was any metallicity dependence in the mass function. In order to test this, we split the sample into three metallicity bins, a high-metallicity bin ([Fe/H] $\geq +0.2$ dex), an intermediate metallicity bin ($-0.1 \leq$ [Fe/H] $< +0.2$ dex), and a low-metallicity bin ([Fe/H] < -0.1 dex). These bin sizes allowed a useful number of samples in each bin to statistically probe the distributions.

Metallicity splitting gives us probabilities (D-statistics) from two-tailed KS-tests of 8 per cent (0.165) that the high-metallicity bin and the low-metallicity bin are drawn from the same parent population, and 6 per cent (0.161) that the intermediate metallicity planet-hosts and the low-metallicity planet-hosts are also drawn from the same population. By combining the high-metallicity bin and the low-metallicity bin values and comparing those to the intermediate metallicity bin, the probability is essentially the same, only dropping the D-statistic by 0.01, with a probability of only 6 per cent that the two populations are statistically similar. To perform this test, we decided to remove the lowest mass planets from the metal-poor and intermediate-metallicity samples since Jenkins et al. (2013b) shows that there appears to be a correlation between the mass and metallicity in the low-mass regime. Therefore, we only consider planets with minimum masses above 0.0184 M_J as this is the lowest mass planet in the high-metallicity sample, neglecting the exceptional case of the planet orbiting Alpha Centauri B (Dumusque et al. 2012) that Hatzes (2013) and Rajpaul et al. (2015) claim may be attributed to other phenomena like stellar activity or sampling ghosts.

In order to firm up these statistics, we also ran the samples through the Anderson–Darling (AD) test, which generally tends to be more sensitive than the standard KS test since it gives more statistical weight to the tails of the distribution. From these tests, we found p-values of 2 and 5 per cent for the comparison between the high- and low-metallicity samples, and between the intermediate- and low-metallicity samples, respectively. This is in good agreement with the KS test results, indicating that there is a correlation between mass and metallicity, whereby metal-rich stars produce many more Jupiter-mass planets compared to super-Jupiters, but metal-poorer stars produce a higher fraction of super-Jupiters than Jupiters compared to the metal-rich population. However, the current sample of host star properties were not drawn from a homogeneous source and therefore the heterogeneous nature of the data could be influencing the results.

To try to circumvent this problem, we decided to search for our sample of exoplanet-hosts in the SWEET-Cat catalogue (Santos et al. 2013). The SWEET-Cat is a project that plans to eventually contain all exoplanet-host star properties like $T_{\rm eff}$ and metallicity that have been measured using high-resolution spectroscopy in a homogeneous fashion. We were able to find 93 per cent of our sample in the SWEET-Cat, but some of these were not measured homogeneously. From this sample, we reran the KS tests and found probabilities of 9.1 per cent that the high- and low-metallicity bins are drawn from the same parent population and 13.8 per cent that the intermediate- and low-metallicity bins are drawn from the same distribution.

A further step that was taken was to remove even more information but improve the homogeneity of the sample. We selected only those stars with a homogeneous flag of 1 in the SWEET-Cat, which means that the properties of these stars were measured using the same general methodology. This selection resulted in a 20 per cent loss of information but still contained a total sample size of 358 planet-hosts, however the low-metallicity bin only contained 64 stars, whereas the high and intermediate bins have sample sizes of 131 and 163 objects, respectively. The KS test probabilities are now significantly lower than the full sample, having values of 38.0 and 52.0 per cent that the high- and intermediate-mass functions are statistically similar to that of the low-metallicity bin. These tests likely show that currently there are no statistically significant correlations between planetary mass and the metallicity of their host stars, as claimed by Mortier et al. (2012), and the overabundance of Jupiter's is not due to the enhanced formation of such planets as a function of metallicity. We did not run the SWEET-Cat samples through the AD test since the results were shown to be very similar to the KS tests for the full sample.

4.3 Other observational properties

Within the period-mass plane, some features can be seen in the metallicities of exoplanet-host stars. An examination of the left plot in Fig. 16 reveals that there is a broad mix of metallicities for the gas giant planets and the planets we publish here are located predominantly in the upper-right quadrant of the plot, with only two having periods below 100 d.

4.3.1 Host star metallicities

It appears that the lowest mass planets are found mostly on short-period orbits, due to the inherent sensitivities of Doppler surveys, and they also appear to orbit metal-poor stars in general, hence the dominance of the black points towards the bottom left of the left-hand panel in Fig. 16. This result was previously highlighted by Jenkins et al. (2013b), revealing a 'planet desert' for the most metal-rich stars, and subsequent confirmation has also been discussed in Marshall et al. (2014). The nature of this desert could be explained by core accretion theory whereby the lower density discs have limited metals to form cores, whereas the high-density discs can readily form high-mass cores that quickly grow to more massive objects, crossing the critical core mass limit and becoming gas giants. In fact, the metallic properties of all planets with periods of less than 100 d appears to be different when we compare planets

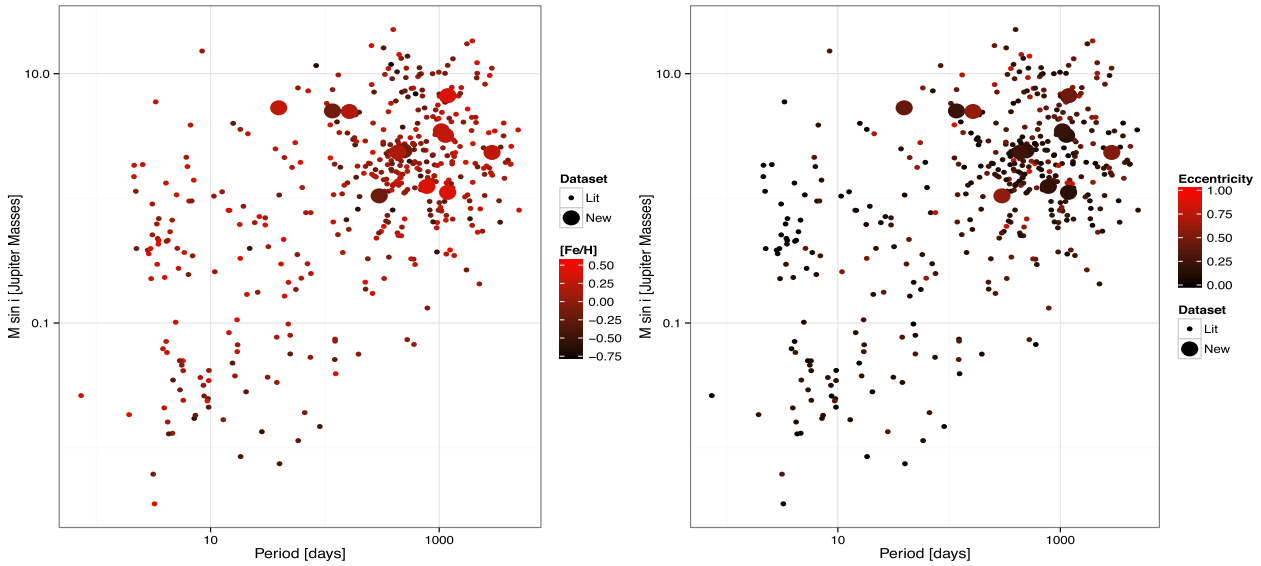

Figure 16. Distribution of exoplanet metallicities (left) and eccentricities (right) within the period-mass plane. The small circles are the literature values and the large circles are our targets from this work. The colour scale to highlight the differing metallicities and eccentricities are shown at the right of both plots.

more massive or less massive than 0.1 M_J. In the plot, this is shown by the significantly higher fraction of red data points above a mass of 0.1 M_J compared to below that limit.

More directly, we can test the reality that the metallicity distribution for planets with periods of 100 d or less have a different metallicity distribution by again applying an AD test to the sample of known exoplanets. We chose to apply the sample to the homogeneous samples that we previously cross-matched with the SWEET-Cat list. This test reveals a T-statistic of 8.54 when adjusted for all non-unique values, revealing a probability of 2×10^{-4} that these samples are statistically similar. A Kolmogorov–Smirnov test yields a similar probability value (4×10^{-4}) with a D-statistic of 0.375. The histograms of both populations are shown in the top plot of Fig. 17. Although the two histograms appear to show similar forms, the host stars that contain lower mass planets currently have a flatter shape than the host stars containing higher mass planets in this period space. Although the sample sizes are small, 48 objects in the low-mass population for example, it does appear that the lowest mass planets are drawn from a different metallicity sample when compared with the most massive planets, within the limits of the current data set. In the future with many more discoveries of very low mass planets orbiting the nearest stars from Doppler surveys, since these represent the most precise metallicities that can be measured, trends such as those discussed here can be tested at a higher level of statistical significance.

Further to this, the high-mass planet sample may indicate there is a non-uniform metallicity distribution as a function of period. To test this, we split the high-mass planet sample into two bins with orbital periods less than or equal to 100 d and those beyond 100 d. The binned histogram for both samples is shown in the lower plot of Fig. 17, and although the distributions appear less discrepant than the mass cut in the top plot, there is an indication of a functional change in the metal-poor regime. The AD test of the metallicities from these samples returns a T-statistic of 7.62, leading to a probability of 4×10^{-4} that the samples are similar. This time the Kolmogorov–Smirnov test reveals a slightly smaller probability of the null hypothesis, returning a value of 8×10^{-3} and a D-statistic of 0.223. Therefore, we find that, in general, short-period giant planets have higher metallicities than those at longer periods,

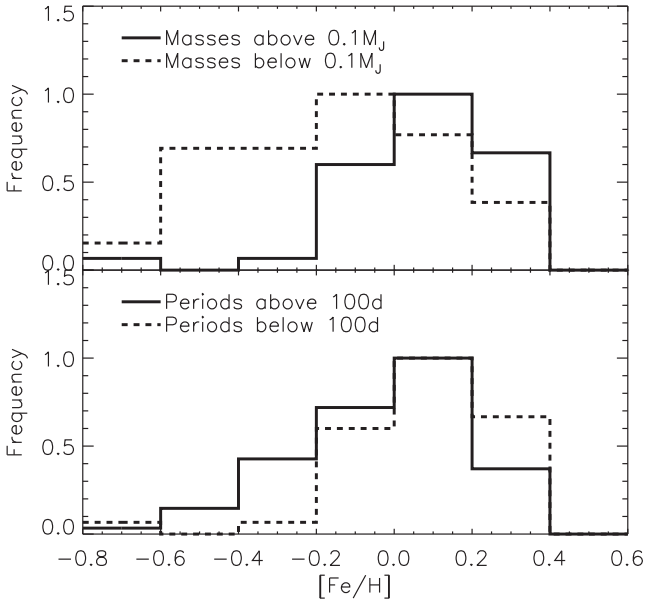

Figure 17. The binned histogram of sub-100 d period exoplanet-host star metallicities detected by RV programmes is shown in the top plot. The solid histogram represents the gas giant planets, minimum masses above 0.1 M_J, and the dashed histogram is for host stars with planets below this threshold. The lower plot shows the binned histogram of gas giant planets (minimum masses above 0.1 M_J) for orbital periods of 100 d or less (solid histogram) and those with periods above 100 d (dashed histogram). All histograms have been normalized to the peak of the distribution to highlight their differences.

with a mean value of [Fe/H] of 0.16 dex for the sub-100 d planets and a value of 0.06 dex for the giant planets with orbital periods longer than 100 d, as suggested by Sozzetti (2004) and Pinotti et al. (2005).

Mordasini et al. (2012) constructed global population synthesis models of forming planets in a range of disc environments to search for expected correlations between planetary orbital parameters and bulk compositions against disc properties. They found that planets tend to migrate more in low-metallicity discs compared to more

metal-rich discs because the cores that form in the low-metallicity environment need to migrate more to undergo enough collisions to grow to the critical mass limit and transition from Type I migration to the slower Type II migration. They suggest that no clear correlation between the semimajor axis, or the orbital period, exists because the planets in low-metallicity discs also form further from the central star than in the high-metallicity discs, and so the increased efficiency of migration in the low-metallicity environment is compensated by the increased distance the planets need to travel inwards towards the star.

These modelling efforts tend to be at odds with the findings we have made unless certain conditions apply. If giant planets in metal-poor discs migrate more, then we would expect to see the opposite result, unless the planets start their journeys very far out in the disc before arriving at their current locations. In addition, another scenario could be that the low-metallicity discs are dispersed faster than high-metallicity discs through photoevaporation (Yasui et al. 2009; Ercolano & Clarke 2010). This effect is thought to be due to the lower optical depth of the disc allowing the UV and X-ray flux to pass deeper into the disc, dispersing the inner regions faster, meaning there is no remaining gas and dust for the planet to interact with, essentially halting its migration earlier when compared to a planet migrating through a metal-rich disc. Finally, in the Mordasini et al. model, they predominantly consider mostly inward migration of cores, however recent work has shown that disc structure is important in defining the dominant torques that drive planet migration and in the inner discs that are heated by the intensity of the young star's radiation field, corotation torques dominate over the differential Linblad torques, leading to outward migration of the cores (Kretke & Lin 2012). Further to this, random walk motion too can be important for migrating low-mass cores (Laughlin, Steinacker & Adams 2004; Nelson & Papaloizou 2004; Nelson 2005) and dead-zones in the disc can subsequently halt the migration of forming low-mass cores (Balmforth & Korycansky 2001; Li et al. 2009; Yu et al. 2010). All of these processes could lead to the preservation of a period–metallicity relationship that favours short-period planets predominantly being found orbiting more metal-rich stars and longer period planets being found in more metal-poor environments.

4.4 Orbital eccentricities

In the right plot in Fig. 16, we show the same period-minimum mass plane, yet this time the colour scaling highlights the eccentricity distribution. We can see that the majority of the short-period planets ($P \leq 10$ d) are generally found to have circular orbits, a fact that can be attributed to the planets tidal interactions with the host star that tends to circularize their orbits. We also see that the majority of the low-mass planets are found on circular orbits too (black points), in comparison to the high-mass planets where a significant fraction of them have moderate-to-high eccentricities (red points). Note that there is also a selection bias towards the detection of higher eccentricities that depends on the quantity of RV data points that describes a given signal (O'Toole et al. 2009), whilst high eccentricity also elevates the amplitude of a given Doppler signal, which can sometimes make them easier to detect.

If we again split the planets up into two mass bins, where the low-mass planets have minimum masses of $\leq 0.1\ M_{\rm J}$ and the high-mass bin comprises all planets with minimum masses above this limit, the eccentricity means and standard deviations of the two populations are 0.13 and 0.12 for the low-mass planet population and 0.25 and 0.21 for the high-mass planet sample. Taken at face value, the increased standard deviation for the higher mass sample tells us the spread in eccentricities in this mass regime is higher than for the lower mass planets. There is a strong bias here where the low-mass planet sample has a significantly lower mean orbital period, with a much higher fraction of planets orbiting close enough to the star to be quickly circularized through tidal dissipation of the orbits. Furthermore, there is a tendency to fix the eccentricity to zero when performing Keplerian fits to RV data, in order to remove this additional degree of freedom and the degeneracy with other parameters being fit at the same time.

5 SUMMARY

We have used the CORALIE, HARPS and MIKE spectrographs to discover eight new giant planets orbiting seven supermetal-rich stars, and a star of solar metallicity, along with updated orbits for four previously published planets. We include RV data prior- and post-2014 CORALIE upgrade and our Bayesian updating method returned a systematic offset of 19.2 ± 4.8 m s^{-1} between the two velocity sets for our stars. The new planets cover a wide area of the giant planet parameter space, having a range of masses, periods, and eccentricities, including a double planet system that was found orbiting the most massive star in our list, and a 14 Herculis *b* analogue that has a minimum mass of $\sim$5.5 $M_{\rm J}$, an orbital period of nearly 1200 d, and significant eccentricity ($e = 0.46$), adding another member to the subpopulation of massive eccentric planets orbiting supermetal-rich stars.

We introduced our method for measuring the chromospheric *S*-index that is a measure of the magnetic activity of Sun-like stars using CORALIE spectra. These activities, along with bisector measurements, CCF FWHM's, Hα indices, H I indices, and *Hipparcos* and ASAS photometry, were used to rule out the origin of the planetary Doppler signal as being due to line modulations from rotationally influenced star spot migration or other activity phenomena like chromospheric plage or stellar pulsations.

We show that the mass function for planets is well described by an exponential function with a scaling parameter of 0.89 ± 0.03 and an offset of $0.030^{+0.004}_{-0.003}$. We confirm the lack of the lowest mass planets orbiting metal-rich stars and we also find a period–metallicity correlation for giant planets. The population of planets with masses $\geq 0.1\ M_{\rm J}$ and orbital periods less than 100 d is found to be more metal-rich than the same mass planets with orbital periods greater than 100 d. The difference is significant at the 0.004 per cent level and the mean difference is found to be 0.16 dex between the two populations. This result could be describing the formation locations of planets in the early discs, with metal-rich discs forming planets in the inner regions and metal-poor discs forming planets further out in the disc, or that giant planets migrate more in metal-rich discs, due to a stronger torque interaction between the high surface density disc and the migrating planet.

ACKNOWLEDGEMENTS

We thank the anonymous referee for providing a fair and helpful report. We are also thankful for the useful discussions with Francois Menard and to Andres Jordán for providing access to the CORALIE pipeline. JSJ acknowledges funding by Fondecyt through grants 1161218 and 3110004, partial support from CATA-Basal (PB06, Conicyt), the GEMINI-CONICYT FUND and from the Comité Mixto ESO-GOBIERNO DE CHILE, and from the Conicyt PIA Anillo ACT1120. MJ acknowledges financial support from Fondecyt project #3140607. DM is supported by the BASAL CATA Center for Astrophysics and Associated

Technologies through grant PFB-06, by the Ministry for the Economy, Development, and Tourism's Programa Iniciativa Científica Milenio through grant IC120009, awarded to Millennium Institute of Astrophysics (MAS), and by FONDECYT Regular grant no. 1130196. This research has made use of the SIMBAD data base and the VizieR catalogue access tool, operated at CDS, Strasbourg, France.

REFERENCES

Anglada-Escudé G., López-Morales M., Chambers J. E., 2010, ApJ, 709, 168
Anglada-Escudé G. et al., 2013, A&A, 556, A126
Arriagada P., Butler R. P., Minniti D., López-Morales M., Shectman S. A., Adams F. C., Boss A. P., Chambers J. E., 2010, ApJ, 711, 1229
Bakos G. Á. et al., 2013, PASP, 125, 154
Balmforth N. J., Korycansky D. G., 2001, MNRAS, 326, 833
Baranne A. et al., 1996, A&AS, 119, 373
Buchhave L. A., Latham D. W., 2015, ApJ, 808, 187
Butler R. P., Marcy G. W., Williams E., McCarthy C., Dosanjh P., Vogt S. S., 1996, PASP, 108, 500
Butler R. P., Marcy G. W., Vogt S. S., Fischer D. A., Henry G. W., Laughlin G., Wright J. T., 2003, ApJ, 582, 455
Butler R. P. et al., 2006, ApJ, 646, 505
Dawson R. I., Fabrycky D. C., 2010, ApJ, 722, 937
Demarque P., Woo J.-H., Kim Y.-C., Yi S. K., 2004, ApJS, 155, 667
Dumusque X. et al., 2012, Nature, 491, 207
Ercolano B., Clarke C. J., 2010, MNRAS, 402, 2735
Fischer D. A., Valenti J., 2005, ApJ, 622, 1102
Foreman-Mackey D., Hogg D. W., Lang D., Goodman J., 2013, PASP, 125, 306
Foreman-Mackey D., 2016, J. Open Source Software, 24
Haario H., Saksman E., Tamminen J., 2001, Bernoulli, 7, 223
Haario H., Laine M., Mira A., Saksman E., 2006, Stat. Comput., 16, 339
Hatzes A. P., 2002, Astron. Nachr., 323, 392
Hatzes A. P., 2013, ApJ, 770, 133
Høg E. et al., 2000, A&A, 355, L27
Ida S., Lin D. N. C., 2004, ApJ, 604, 388
Isaacson H., Fischer D., 2010, ApJ, 725, 875
Ivanyuk O., Jenkins J., Pavlenko Y., Jones H., Pinfield D., 2016, MNRAS, in press
Jenkins J. S., Tuomi M., 2014, ApJ, 794, 110
Jenkins J. S. et al., 2006, MNRAS, 372, 163
Jenkins J. S., Jones H. R. A., Pavlenko Y., Pinfield D. J., Barnes J. R., Lyubchik Y., 2008, A&A, 485, 571
Jenkins J. S. et al., 2009, MNRAS, 398, 911
Jenkins J. S. et al., 2011a, in Martin E.L., Ge J., Lin W., eds, EPJ Web Conf., 16, Research, Science and Technology of Brown Dwarfs and Exoplanets. EDP Sciences, p. 2004
Jenkins J. S. et al., 2011b, A&A, 531, A8
Jenkins J. S. et al., 2013a, in Saglia R., ed., EPJ Web Conf., 47, Hot Planets and Cool Stars. EDP Sciences, p. 5001
Jenkins J. S. et al., 2013b, ApJ, 766, 67
Jenkins J. S., Tuomi M., Brasser R., Ivanyuk O., Murgas F., 2013c, ApJ, 771, 41
Jenkins J. S., Yoma N. B., Rojo P., Mahu R., Wuth J., 2014, MNRAS, 441, 2253
Jones H. R. A., Butler R. P., Tinney C. G., Marcy G. W., Carter B. D., Penny A. J., McCarthy C., Bailey J., 2006, MNRAS, 369, 249
Jones M. I., Jenkins J. S., Bluhm P., Rojo P., Melo C. H. F., 2014, A&A, 566, A113
Jones M. I. et al., 2016, A&A, 590, A38
Jordán A. et al., 2014, AJ, 148, 29
Kretke K. A., Lin D. N. C., 2012, ApJ, 755, 74
Laughlin G., Steinacker A., Adams F. C., 2004, ApJ, 608, 489
Li H., Lubow S. H., Li S., Lin D. N. C., 2009, ApJ, 690, L52
Lo Curto G. et al., 2010, A&A, 512, A48
Lopez S., Jenkins J. S., 2012, ApJ, 756, 177
López-Morales M. et al., 2008, AJ, 136, 1901
Marcy G. W., Butler R. P., 1996, in Kingsley S. A., Lemarchand G. A., eds, Proc. SPIE Conf. Ser. Vol. 2704, The Search for Extraterrestrial Intelligence (SETI) in the Optical Spectrum II. SPIE, Bellingham, p. 46
Marcy G. W., Butler R. P., Fischer D., Vogt S. S., Lissauer J. J., Rivera E. J., 2001, ApJ, 556, 296
Marsakov V. A., Shevelev Y. G., 1988, Bull. Inf. Cent. Donnees Stellaires, 35, 129
Marsh T. R., 1989, PASP, 101, 1032
Marshall J. P. et al., 2014, A&A
Mayor M., Queloz D., 1995, Nature, 378, 355
Meschiari S., Wolf A. S., Rivera E., Laughlin G., Vogt S., Butler P., 2009, PASP, 121, 1016
Minniti D., Butler R. P., López-Morales M., Shectman S. A., Adams F. C., Arriagada P., Boss A. P., Chambers J. E., 2009, ApJ, 693, 1424
Mizuno H., 1980, Prog. Theor. Phys., 64, 544
Mordasini C., Alibert Y., Benz W., Klahr H., Henning T., 2012, A&A, 541, A97
Mortier A., Santos N. C., Sozzetti A., Mayor M., Latham D., Bonfils X., Udry S., 2012, A&A, 543, A45
Murgas F., Jenkins J. S., Rojo P., Jones H. R. A., Pinfield D. J., 2013, A&A, 552, A27
Nelson R. P., 2005, A&A, 443, 1067
Nelson R. P., Papaloizou J. C. B., 2004, MNRAS, 350, 849
Nelson B. E., Robertson P. M., Payne M. J., Pritchard S. M., Deck K. M., Ford E. B., Wright J. T., Isaacson H. T., 2016, MNRAS, 455, 2484
Newton M. A., Raftery A. E., 1994, J. R. Stat. Soc. B, 56, 3
O'Toole S. J., Tinney C. G., Jones H. R. A., Butler R. P., Marcy G. W., Carter B., Bailey J., 2009, MNRAS, 392, 641
Pavlenko Y. V., Jenkins J. S., Jones H. R. A., Ivanyuk O., Pinfield D. J., 2012, MNRAS, 422, 542
Pepe F., Mayor M., Galland F., Naef D., Queloz D., Santos N. C., Udry S., Burnet M., 2002, A&A, 388, 632
Perryman M. A. C. et al., 1997, A&A, 323, L49
Pinotti R., Arany-Prado L., Lyra W., Porto de Mello G. F., 2005, MNRAS, 364, 29
Pojmanski G., 1997, Acta Astron., 47, 467
Queloz D. et al., 2001, A&A, 379, 279
Rajpaul V., Aigrain S., Osborne M. A., Reece S., Roberts S. J., 2015, MNRAS, 452, 2269
Reffert S., Bergmann C., Quirrenbach A., Trifonov T., Künstler A., 2015, A&A, 574, A116
Robertson P., Mahadevan S., Endl M., Roy A., 2014, Science, 345, 440
Saar S. H., Donahue R. A., 1997, ApJ, 485, 319
Santos N. C., Israelian G., Mayor M., 2004, A&A, 415, 1153
Santos N. C., Gomes da Silva J., Lovis C., Melo C., 2010, A&A, 511, A54
Santos N. C. et al., 2013, A&A, 556, A150
Soto M. G., Jenkins J. S., Jones M. I., 2015, MNRAS, 451, 3131
Sousa S. G., Santos N. C., Israelian G., Mayor M., Udry S., 2011, A&A, 533, A141
Sozzetti A., 2004, MNRAS, 354, 1194
Takeda G., Ford E. B., Sills A., Rasio F. A., Fischer D. A., Valenti J. A., 2007, ApJS, 168, 297
Tamuz O. et al., 2008, A&A, 480, L33
Tuomi M., 2012, A&A, 543, A52
Tuomi M., 2014, MNRAS, 440, L1
Tuomi M., Anglada-Escudé G., 2013, A&A, 556, A111
Tuomi M. et al., 2013, A&A, 551, A79
Tuomi M., Jones H. R. A., Barnes J. R., Anglada-Escudé G., Jenkins J. S., 2014, MNRAS, 441, 1545
Udry S. et al., 2007, A&A, 469, L43
Valenti J. A., Fischer D. A., 2005, ApJS, 159, 141
van Leeuwen F., 2007, A&A, 474, 653
Wittenmyer R. A. et al., 2012, ApJ, 753, 169
Yasui C., Kobayashi N., Tokunaga A. T., Saito M., Tokoku C., 2009, ApJ, 705, 54
Yu C., Li H., Li S., Lubow S. H., Lin D. N. C., 2010, ApJ, 712, 198

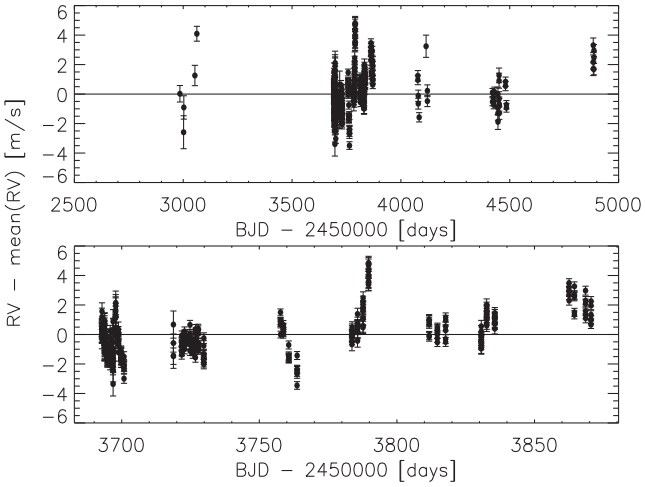

Figure A1. HARPS RV timeseries of HD72673 with the mean subtracted off the data. The upper panel shows the full timeseries and the lower panel is a zoom in on the most densely observed epoch for this star.

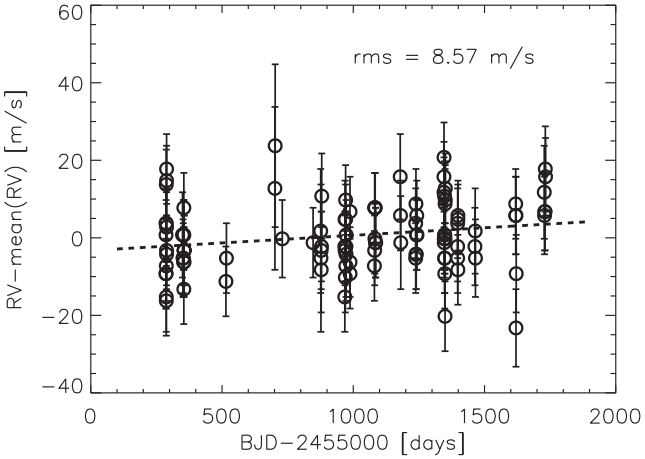

Figure A2. Timeseries and mean subtracted radial velocities for the star HD72673. The dashed line represents the best straight line fit to the data. The rms scatter around the fit in m s^{-1} is shown in the plot.

APPENDIX A: STABLE STAR RESULTS

To confirm the stability of the CORALIE pipeline reduction and analysis procedure, we have observed a star known to be RV stable at the ∼2 m s^{-1} level that should provide an ideal test candidate for our method. HD72673 is a bright ($V = 6.38$), nearby (12.2 pc), and inactive ($\log R'_{\rm HK} = -4.946$; Isaacson & Fischer 2010) G9 dwarf star that has a metallicity of -0.38 ± 0.04 dex (Marsakov & Shevelev 1988; Santos, Israelian & Mayor 2004; Valenti & Fischer 2005), and a mass and age of 0.814 ± 0.032 M$_\odot$ and $1.48^{+5.44}_{-1.48}$ Gyr (Takeda et al. 2007), respectively.

In the upper panel of Fig. A1, we show the RV timeseries for HD72673 observed with HARPS that was taken from the ESO Archive.[1] The data span a baseline of over 1900 d in total and comprise 363 individual RV measurements where we have removed 5σ outliers that corresponded to bad weather observations, and therefore had very low S/N data, like the point at BJD-2453724.79378. After subtracting off the mean of the data, which we use as our standard flat noise model, we find an rms of 1.44 m s^{-1}. The lower panel shows the same data except zoomed in on the most densely sampled observing epoch (BJD 2453500−2454000). Some structure is found in the radial velocities throughout this epoch and could be the first signatures of low-amplitude Doppler shifts induced by orbiting low-mass planets, or stellar activity signals affecting the velocities. In any case, the HARPS velocities agree that HD72673 does not show large RV variations and is a useful star for testing the precision we can achieve with our CORALIE pipeline.

[1] Based on data obtained from the ESO Science Archive Facility under request number JJENKINS 50958.

A1 CORALIE observations

Over the course of 4 yr, we have performed 108 observations of the star HD72673 with CORALIE, combining data from this project and also from the HAT-South (Bakos et al. 2013) CORALIE observations. The sampling and time baseline provide an excellent diagnostic test of the long-term stability that is currently attained with the CORALIE using the procedure described in Jordán et al. (2014).

For the observations of HD72673, we aimed to get an S/N of around 100 across the optical regime of interest, leading to typical integration times of ∼5 min. Fig. A2 shows the full RV data set as a function of time and clearly we see only a small linear trend over the full baseline of observations. No large systematic trends are found in our data set and the gradient of the best fit we show is 0.004 m s^{-1} d^{-1}, well below the intrinsic scatter of our procedure. The rms scatter for the full data is found to be 10.9 m s^{-1}, however after removing a 5σ outlier due to low S/N we arrive at a scatter of 8.7 m s^{-1}, or 8.6 m s^{-1} after subtraction of the linear trend shown in the figure. Therefore, we consider the precision of the CORALIE observations to be 9 m s^{-1}, consistent with the precision reported by Jordán et al., but covering a longer time baseline.

APPENDIX B: MMSE PERIODOGRAMS

The MMSE periodograms from the RV timeseries data discussed in this work. The vertical dashed lines mark the signals detected by the MCMC search algorithm.

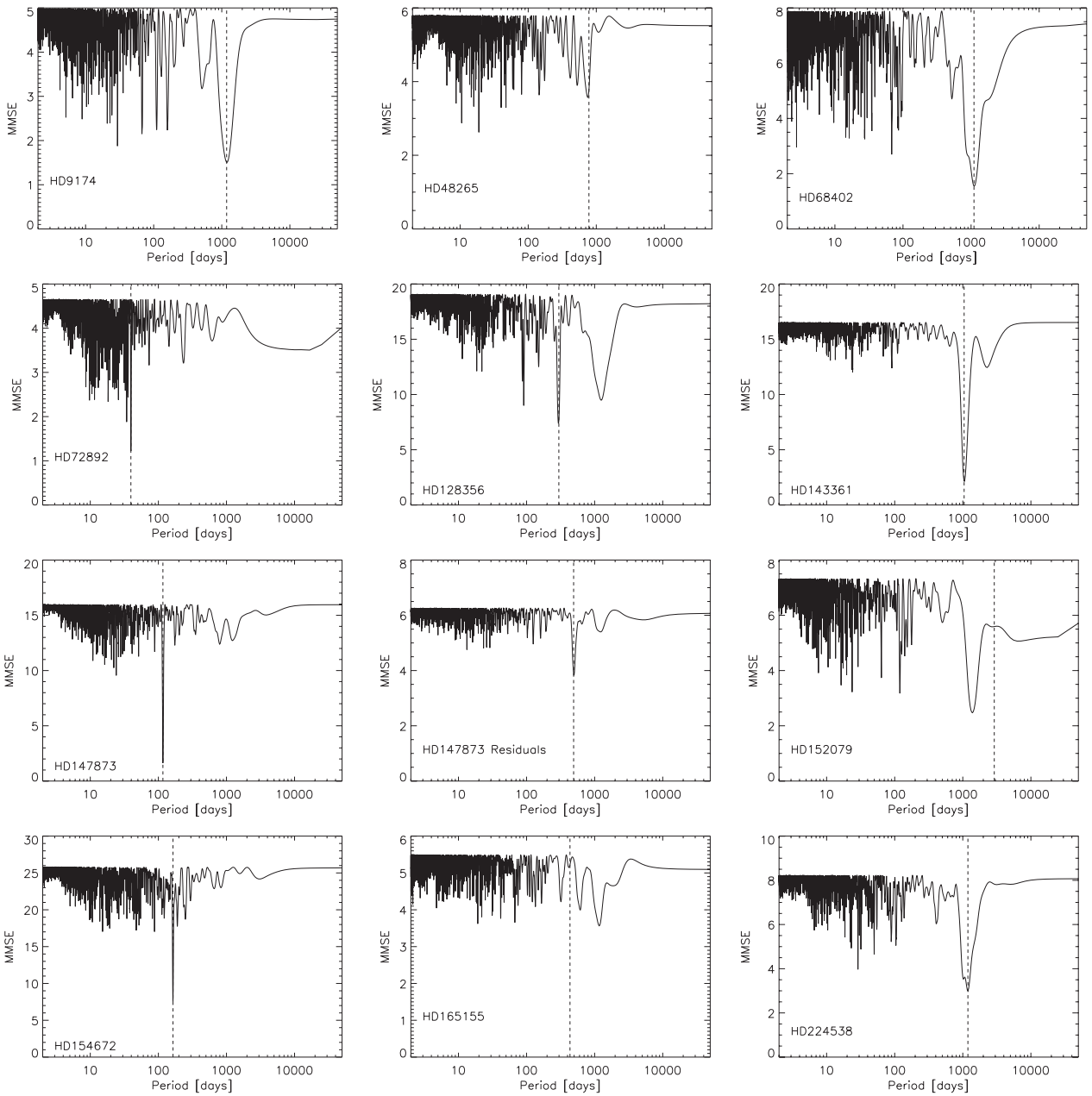

Figure B1. Periodograms from top left to bottom right: HD9174, HD48265, HD68402, HD72892, HD128356, HD143361, HD147873, HD147873 residuals after fitting out the best-fitting Keplerian signal associated with the raw data primary spike, HD152079, HD154672, HD165155, and HD224538. The dashed vertical lines represent the periods detected by the MCMC analysis.

APPENDIX C: MCMC POSTERIOR DENSITIES

Here, we show the posterior densities from our MCMC search for signals in the radial velocities for all targets in this work. We show the densities from the samplings for the periods, semiamplitudes, and eccentricities for all signals.

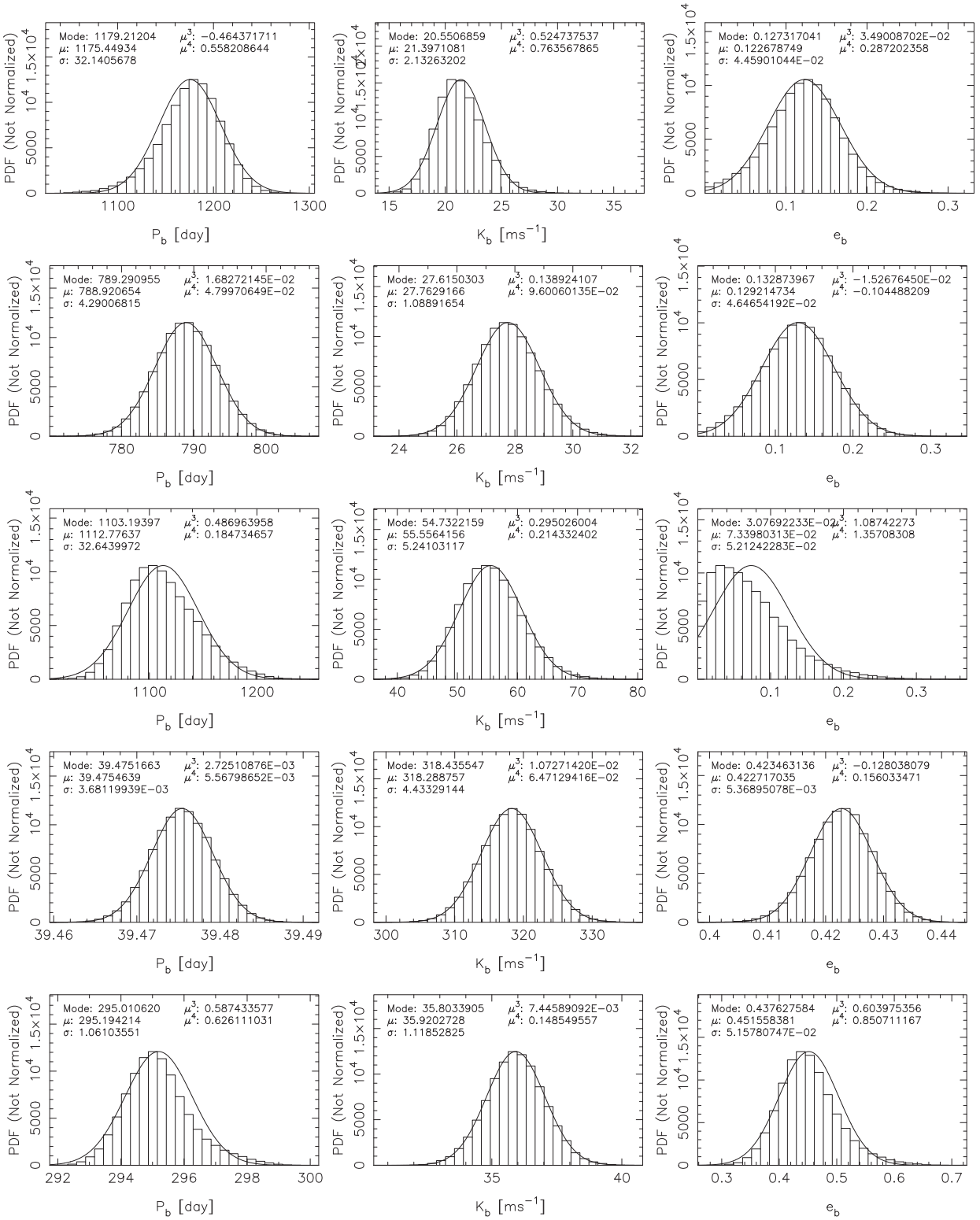

Figure C1. Posterior densities for the signals HD9174*b*, HD48265*b*, HD68402*b*, HD72892*b*, and HD128356*b*.

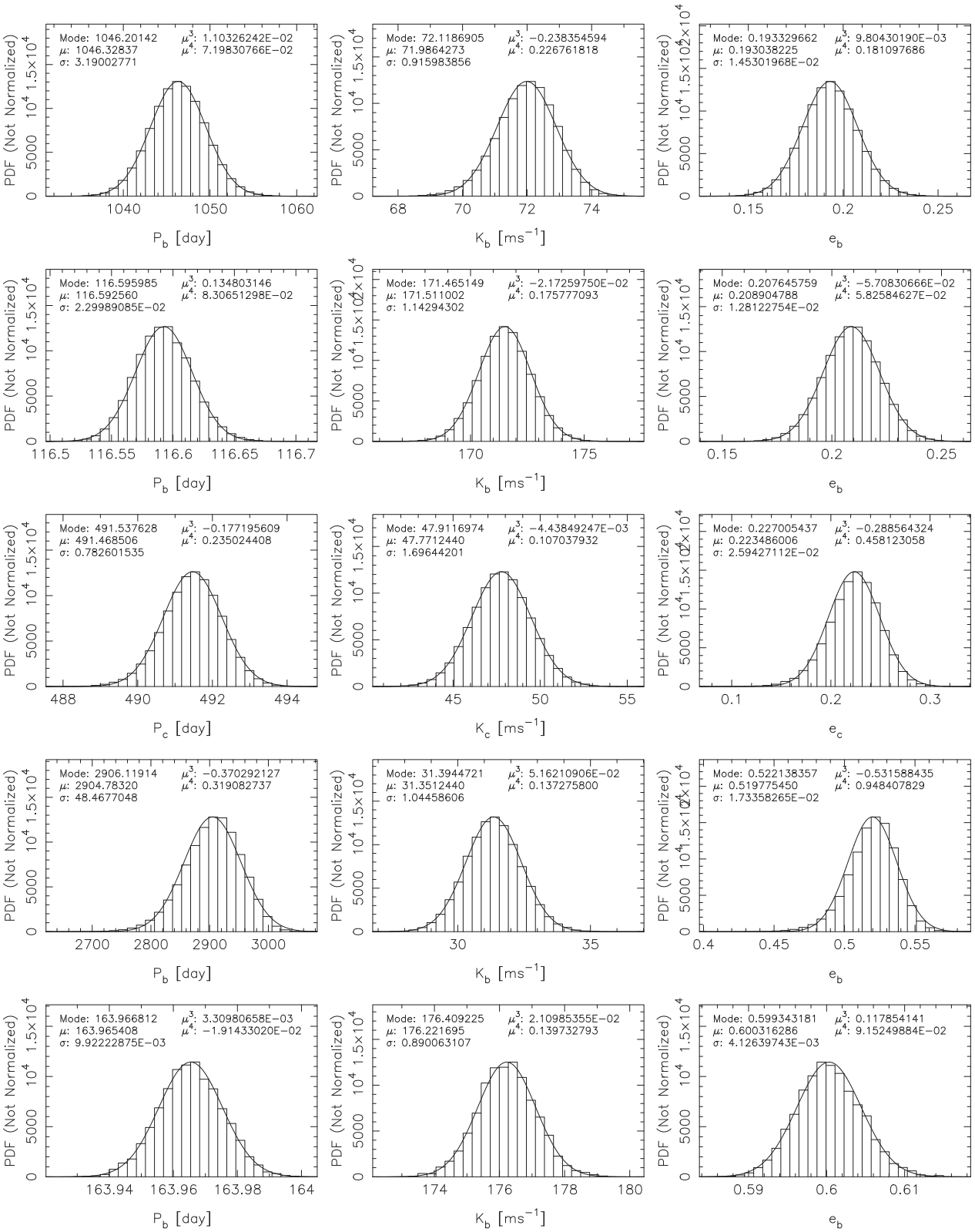

Figure C2. Posterior densities for the signals HD143361*b*, HD147873*b*, HD147873*c*, HD152079*b*, and HD154672*b*.

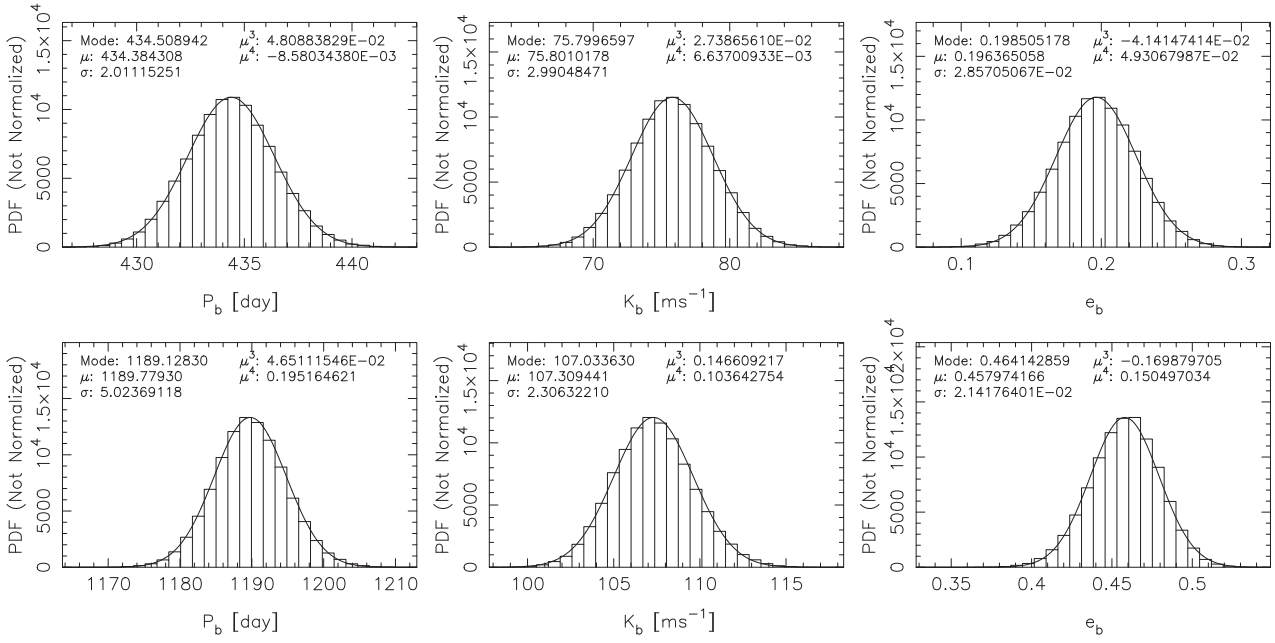

Figure C3. Posterior densities for the signals HD165155*b* and HD224538*b*.

APPENDIX D: CORALIE CHROMOSPHERIC ACTIVITY INDICES

We measure the CORALIE activities using only four echelle orders, even though the regions we require for the $S_{\rm MW}$ passbands are found across five orders. We drop one of the orders (order 4) due to an excess of noise at the blue end, which is due to the position of the echellogram where the *V* passband is found and therefore including this order enhances the uncertainty in the *S*-index and, in general, artificially increases the activity value making each star appear more active than it really is. We note that this could be taken out by calibration to other chromospheric indexes. We show the CORALIE extraction regions in Fig. D1 .

We compute the activities by integrating the square continuum *V* (3891–3911 Å) and *R* (3991–4011 Å) bandpasses and taking the ratio of these against the integrated flux in the triangular core bandpasses, described in the following series of equations:

$$f_{j,i} = \Im_{j,i} * B_{j,i} * \delta\lambda \tag{D1}$$

$$S_{\rm cont} = \frac{\sum (f_{V,i} + f_{R,i})}{\sum (B_{V,i} + B_{R,i}) * \delta\lambda} \tag{D2}$$

$$S_{\rm core} = \frac{\sum (f_{K,i} + f_{H,i})}{\sum (B_{K,i} + B_{H,i}) * \delta\lambda} \tag{D3}$$

$$\sigma_{S_{\rm cont}} = \frac{\sqrt{\sum \left(\sqrt{(\sigma^2_{f_{V,i}} + \sigma^2_{f_{R,i}})}\right)^2}}{\sum (B_{V,i} + B_{R,i}) * \delta\lambda} \tag{D4}$$

$$\sigma_{S_{\rm core}} = \frac{\sqrt{\sum \left(\sqrt{(\sigma^2_{f_{K,i}} + \sigma^2_{f_{H,i}})}\right)^2}}{\sum (B_{K,i} + B_{H,i}) * \delta\lambda}. \tag{D5}$$

The cont and core subscripts represent the continuum and core regions of the spectrum, respectively, $\Im$ is the flux measured in each wavelength domain (*i*), *j* here denotes either the *V*,*R*,*K*, or *H* bandpass regions, and $\delta\lambda$ is the wavelength step (dispersion), which at the resolution of CORALIE is ∼0.023 Å.

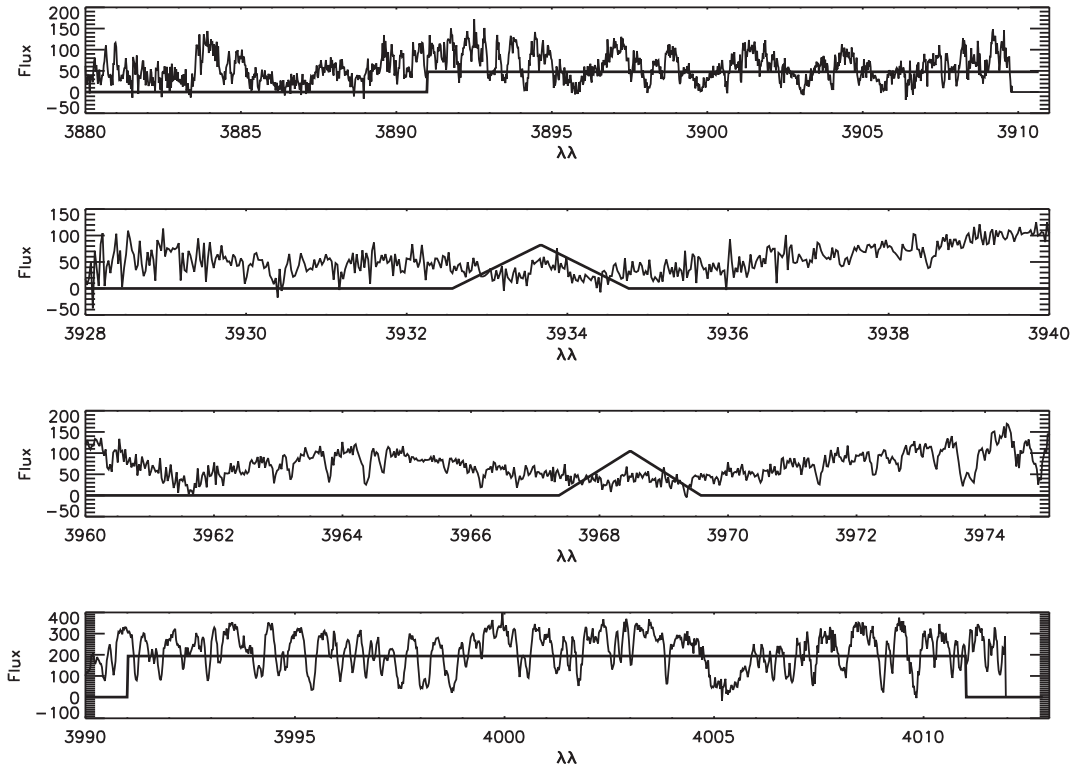

Figure D1. CORALIE echelle orders used to extract the *S* activity indices for HD128356. The square continuum bandpasses regions *V* and *R* are shown by the thick solid lines in the top and bottom plots, respectively. The thick triangular solid lines in the upper and lower centre plots show the *K* and *H* bandpasses, respectively.

APPENDIX E: ACTIVITY INDICATOR PERIODOGRAMS

Lomb–Scargle periodograms of the activity indicators measured from the CORALIE and HARPS timeseries spectra.

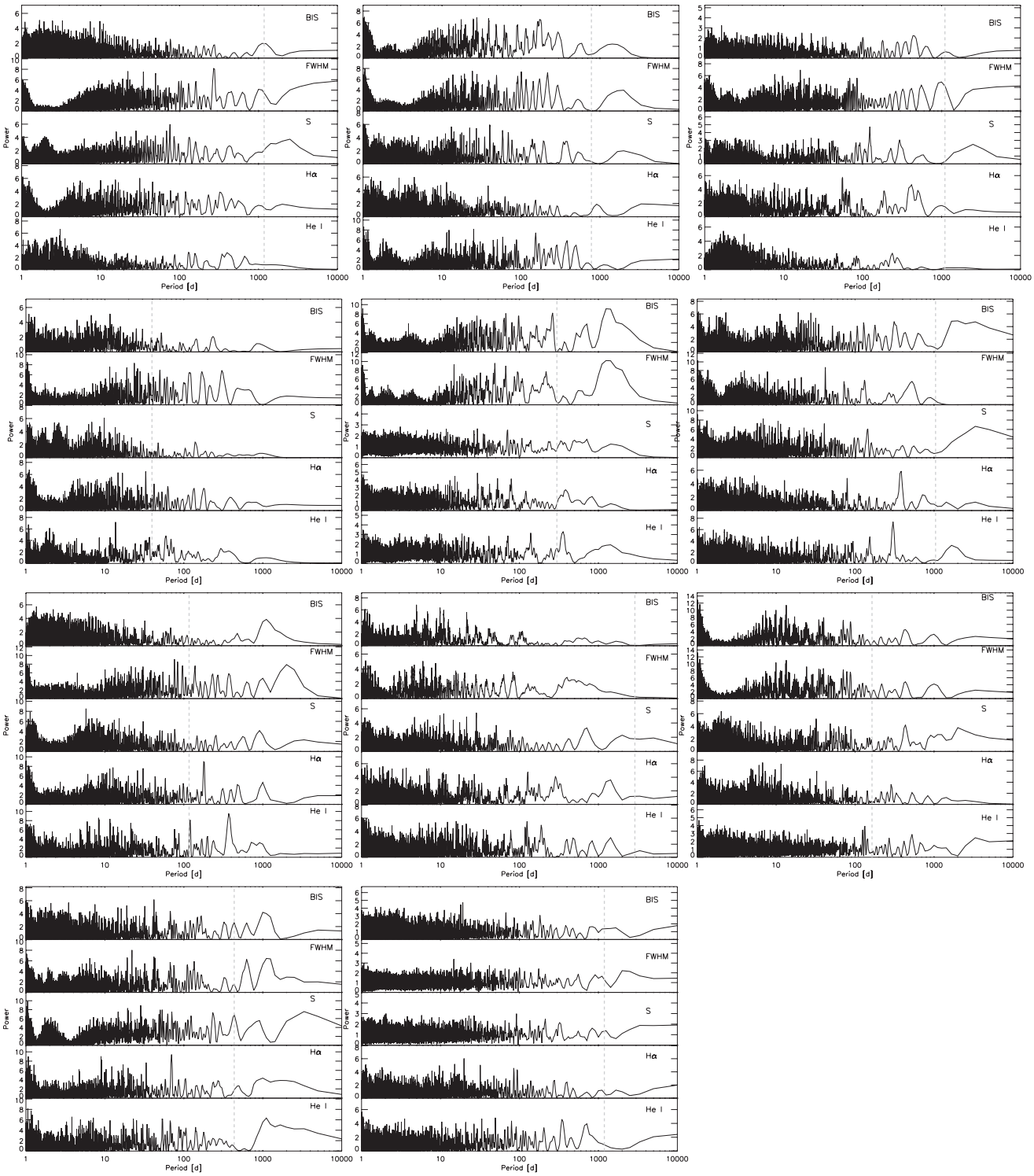

Figure E1. In each plot from top to bottom, we show the periodograms for the BIS, FWHM, *S*, Hα, and H I indices. From top left to bottom right, we show the stars HD9174, HD48265, HD68402, HD72892, HD128356, HD143361, HD147873, HD152079, HD154672, HD165155, and HD224538, respectively.

APPENDIX F: ASAS PERIODOGRAMS

Lomb–Scargle periodograms of the ASAS timeseries *V*-band photometric data for the six stars that show peaks that could be related to magnetic activity on the surface of the star.

APPENDIX G: RADIAL VELOCITIES

Here, we provide all radial velocities that are discussed in this work.

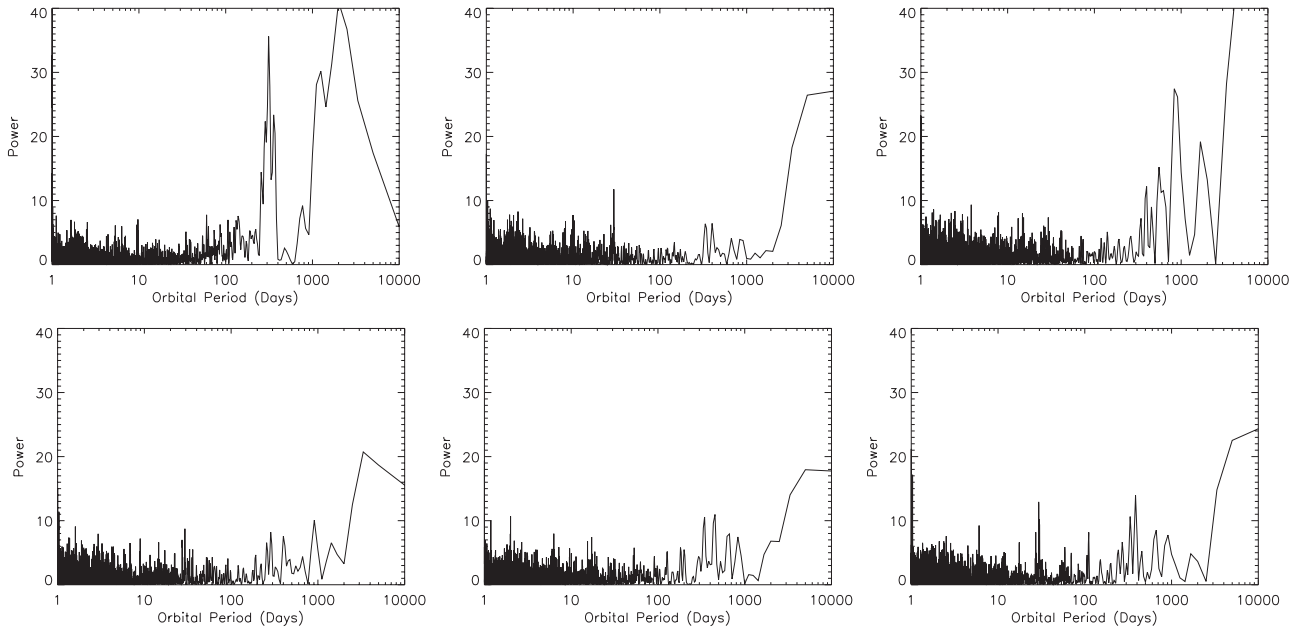

Figure F1. From top left to bottom right, we show the periodograms from ASAS data for the stars HD68402, HD147873, HD152079, HD154672, HD165155, and HD224538, respectively.

Table G1. HD9174.

	CORALIE			HARPS	
BJD	RV	Error	BJD	RV	Error
2455160.5362269	7.2	9.0	2455188.6187049	10.77	0.55
2455161.5372730	− 11.8	9.0	2455883.6145165	− 10.66	0.86
2455162.5377306	30.2	9.0	2455885.5904695	− 12.54	1.03
2455467.6819298	− 35.8	9.0	2456183.7872355	12.43	0.48
2455468.7578863	− 25.8	9.0	2456184.6697746	9.39	0.79
2455878.6618959	− 8.9	9.0	2456184.8402196	8.10	0.92
2455879.6756525	− 5.9	15.0	2456185.7970768	13.90	0.55
2456160.7988170	6.0	9.0	2456442.9352036	3.98	0.69
2456164.7903294	38.0	9.0	2456461.9331703	0.26	0.74
2456307.5567717	23.0	9.0	2456463.8950719	1.48	0.77
2456308.5698681	20.0	9.0	2456561.7814364	− 13.46	0.50
2456675.6083797	− 22.0	9.0	2456562.5748725	− 12.24	0.86
2456676.6025593	− 16.0	9.0	2456563.6078357	− 13.76	0.78
2456881.8675908	− 20.2	12.0			
2456882.8265879	− 17.2	12.0			
2456883.7721760	− 13.2	12.0			

Table G2. HD48265.

CORALIE			HARPS			MIKE		
BJD	RV	Error	BJD	RV	Error	BJD	RV	Error
2455208.6992489	1.8	9.0	2454365.8248037	− 32.25	0.77	2452920.8629	20.6	6.9
2455209.7264368	10.8	9.0	2454366.8740710	− 25.18	0.99	2453431.6073	− 30.2	2.5
2455210.7165285	− 29.2	9.0	2454367.8521212	− 29.87	0.62	2453455.5573	− 35.0	2.6
2455465.8329696	16.8	9.0	2454580.5231386	22.43	0.64	2453685.8138	15.0	2.9
2455468.8765488	27.8	9.0	2454581.5537085	23.60	0.56	2453774.6744	25.0	3.3
2455877.7963300	− 4.2	15.0	2454724.8337096	− 14.14	0.59	2453775.6763	12.4	5.2
2455878.7843441	13.8	9.0	2454725.8177884	− 13.78	0.53	2453784.6887	25.4	2.6
2455879.7984724	10.8	9.0	2454726.7789038	− 14.84	0.80	2453811.5943	24.3	2.5
2455969.6052648	− 19.2	9.0	2455651.5366350	− 15.41	0.56	2453987.9168	− 7.7	2.9
2455970.7499814	− 17.2	9.0	2455883.7630397	− 7.88	0.70	2454078.7826	− 17.9	3.0
2455971.7266404	− 21.2	9.0	2455885.7426863	− 1.10	0.92	2454081.7133	− 23.4	2.8
2456034.5026492	13.8	9.0	2455992.5816638	18.09	0.56	2454137.6436	− 20.7	2.5
2456037.5096202	37.8	9.0	2455994.5576882	23.81	0.61	2454138.6670	− 28.7	2.6
2456164.8925279	15.8	9.0	2456183.8678319	52.75	0.59	2454189.5669	− 29.5	4.4
2456378.6064455	− 15.2	9.0	2456185.8516258	57.16	0.66	2454483.6148	28.5	3.0
2456379.5444957	− 21.2	9.0	2456442.4578668	− 16.22	0.91	2454501.6725	21.5	2.4
2456380.6001445	− 6.2	9.0	2456444.4478133	− 14.86	1.07	2454522.6219	25.4	2.7
2456381.5979512	− 15.2	9.0	2456562.8313800	− 12.48	0.73			
2456733.6079032	2.9	9.0						
2456736.5950580	19.9	10.0						
2456753.5245324	3.9	10.0						
2456754.5405659	7.9	10.0						

Table G3. HD68402.

CORALIE			HARPS		
BJD	RV	Error	BJD	RV	Error
2455268.5536332	11.4	9.0	2456442.5125503	− 21.04	1.51
2455269.5471815	0.4	9.0	2456444.4892384	− 17.13	1.66
2455270.5544347	4.4	9.0	2456562.9026514	12.99	1.46
2456034.5316938	− 45.6	9.0	2456563.8260976	13.44	1.51
2456037.5405384	− 31.6	9.0	2456563.9098232	11.72	2.07
2456307.7270563	− 32.6	9.0			
2456308.7455901	− 18.6	9.0			
2456675.7326419	47.4	16.0			
2456675.7405950	64.4	17.0			
2456735.5968024	45.0	12.0			
2456736.6337750	33.0	14.0			
2456752.5562350	38.0	13.0			
2456754.5693098	53.0	15.0			
2456823.4935737	33.0	15.0			
2456825.4656166	8.0	12.0			
2457075.6564372	− 43.1	14.0			
2457318.8514672	− 19.1	14.0			

Table G4. HD72892.

	CORALIE			HARPS	
BJD	RV	Error	BJD	RV	Error
2455698.5075694	223.8	9.0	2456442.5223438	− 195.55	1.12
2455699.5368477	337.8	9.0	2456443.5281580	− 167.05	1.77
2455700.5250521	444.8	9.0	2456444.5101783	− 134.83	1.36
2455968.7197064	− 111.2	9.0	2456448.4605785	144.30	1.29
2455969.7048152	− 77.2	9.0	2456449.4624615	248.19	0.82
2455970.6308925	− 55.2	9.0	2456450.4614518	357.16	1.21
2455972.6288495	61.8	9.0	2456462.4520834	− 114.51	1.13
2456034.5646797	− 129.2	9.0	2456463.4499736	− 137.72	1.69
2456037.5717726	− 156.2	9.0			
2456307.7713660	− 110.3	9.0			
2456308.7833076	− 126.3	9.0			
2456378.6598031	159.7	9.0			
2456379.5959537	128.7	9.0			
2456463.4576754	− 57.3	9.0			
2456464.4530818	− 80.3	14.0			
2456465.4567122	− 111.3	9.0			
2456467.4802779	− 147.3	16.0			
2456675.7562736	− 196.3	9.0			
2456734.6035167	134.1	11.0			
2456752.6156272	− 176.9	13.0			
2456754.5855485	− 154.9	13.0			
2456824.4911691	− 138.9	15.0			
2457184.4724902	− 161.0	13.0			

Table G5. HD128356.

	CORALIE			HARPS	
BJD	RV	Error	BJD	RV	Error
2455268.9086205	− 22.1	9.0	2454248.6023117	16.75	1.66
2455269.8196218	− 34.1	9.0	2454248.6108994	21.79	1.69
2455349.6784180	− 16.1	9.0	2454248.6176931	17.99	0.69
2455350.6814856	14.9	9.0	2454367.5031968	− 31.24	0.66
2455351.6612024	− 4.1	9.0	2454369.5091063	− 37.97	2.49
2455352.6667444	− 6.1	9.0	2454577.6158842	35.96	0.48
2455609.8365887	− 27.1	14.0	2454578.5680249	35.50	0.52
2455611.8334577	− 13.1	9.0	2454581.7357981	41.67	0.47
2455699.7015878	9.9	9.0	2455271.8690903	− 23.11	0.36
2455967.8551252	27.9	9.0	2455649.7321937	− 6.46	0.46
2455968.8240257	39.9	9.0	2455650.7148680	− 6.51	0.49
2455970.8305273	20.9	9.0	2455651.7295683	− 7.26	0.50
2455971.7742759	31.9	9.0	2455786.4827996	50.87	0.51
2455972.8507044	46.9	9.0	2455787.4566297	49.97	0.36
2456034.8259987	11.9	9.0	2455992.7730262	9.21	0.39
2456037.8192588	27.9	9.0	2455993.7048066	9.29	0.52
2456160.4758000	− 6.1	9.0	2456063.6469346	34.67	0.78
2456164.4757457	− 9.1	9.0	2456064.6145915	35.94	0.45
2456381.7122851	15.9	9.0	2456065.6564584	36.26	0.43
2456463.5427541	− 23.1	9.0	2456183.4873901	− 31.26	0.60
2456464.6240954	− 35.1	9.0	2456442.6772101	− 46.63	0.46
2456465.6419917	− 45.1	9.0	2456443.6828424	− 46.21	0.77
2456467.5931893	− 26.1	16.0	2456444.6629996	− 45.18	0.91
2456467.6621264	− 24.1	9.0	2456450.4938930	− 40.30	0.62
2456676.8044908	19.8	9.0	2456462.6290393	− 36.01	0.54
2456734.7225188	− 35.2	10.0	2456463.5862333	− 35.50	0.80
2456752.8173417	− 30.2	12.0	2456562.4755850	− 3.37	0.56
2456823.7074373	1.8	14.0			
2456825.7157702	6.8	12.0			
2456881.5522933	4.8	12.0			
2456882.5702439	20.8	15.0			

Table G6. HD143361.

CORALIE			HARPS			MIKE		
BJD	RV	Error	BJD	RV	Error	BJD	RV	Error
2455269.8328453	31.9	12.0	2454253.7711993	10.50	3.17	2452864.57934	43.03	7.14
2455269.8477334	30.9	12.0	2454253.7786414	9.06	2.22	2453130.83712	− 6.28	2.65
2455349.6897288	9.9	14.0	2454367.5565354	− 23.81	1.09	2453872.73696	28.04	2.62
2455349.7090115	6.9	15.0	2454368.5376348	− 23.64	1.13	2453987.50506	38.49	3.45
2455350.6957245	− 5.2	17.0	2454578.7885789	− 83.52	0.83	2453988.49460	25.06	2.81
2455350.7085995	− 11.2	22.0	2454581.8076461	− 81.90	0.92	2454190.80550	0.00	3.43
2455351.6772114	3.9	13.0	2455271.8809609	19.62	0.77	2454217.84734	− 7.02	3.38
2455351.6921046	− 0.2	14.0	2455649.7540214	− 83.51	0.94	2454277.65819	− 29.11	3.43
2455352.6804150	− 8.2	13.0	2455786.5132754	− 30.99	0.89	2454299.55951	− 37.73	3.04
2455352.6925204	2.9	12.0	2455992.7979663	55.69	1.23	2454300.58038	− 36.03	2.51
2455465.4819439	− 37.2	19.0	2455993.7269629	65.78	0.89	2454339.50049	− 52.16	3.39
2455465.4921698	− 41.2	18.0	2456063.6718947	68.27	2.14	2454501.87197	− 94.15	3.01
2455466.4810091	− 44.2	20.0	2456064.6371793	65.24	0.87	2454650.68383	− 105.06	6.82
2455467.4908225	− 36.2	13.0	2456065.6805773	64.11	0.80	2454925.87115	21.04	2.76
2455786.5181546	− 28.2	13.0	2456184.5078021	53.36	0.84	2454963.75707	34.93	3.05
2455787.5128697	− 32.2	12.0	2456442.6901584	− 22.67	0.90	2454965.78744	31.39	2.82
2455788.5005189	− 18.2	12.0	2456443.6959898	− 19.26	1.96	2455019.67861	27.65	2.46
2455967.8637123	48.8	14.0	2456444.7117386	− 20.46	1.79			
2455969.8564628	55.8	14.0	2456462.6564547	− 25.82	0.97			
2455970.8440395	49.8	14.0						
2455971.8236578	61.8	14.0						
2455972.8379866	52.8	14.0						
2456034.8111668	73.8	14.0						
2456037.8046599	73.7	12.0						
2456160.4914594	49.7	11.0						
2456161.4914636	58.7	12.0						
2456162.5761051	53.7	18.0						
2456164.4909267	46.7	12.0						
2456381.7216801	− 14.3	15.0						
2456381.7325023	− 13.3	14.0						
2456463.6056985	− 23.3	12.0						
2456465.6944440	− 22.3	12.0						
2456467.5744277	− 75.3	23.0						
2456554.5120400	− 28.3	16.0						
2456554.5219817	− 49.3	20.0						
2456555.5573278	− 33.3	13.0						
2456676.8679860	− 68.4	14.0						
2456734.7382463	− 61.4	12.0						
2456752.8000194	− 39.4	13.0						
2456754.7548507	− 51.4	13.0						
2456823.7338512	− 33.4	13.0						
2456825.7551623	− 36.4	13.0						
2456881.6125148	5.6	12.0						
2456882.6036411	17.6	15.0						
2457281.5366030	71.5	19.0						

Table G7. HD147873.

CORALIE			HARPS			MIKE		
BJD	RV	Error	BJD	RV	Error	BJD	RV	Error
2455268.8296124	66.7	9.0	2454365.5676419	− 165.09	4.83	2453189.66944	0.00	3.38
2455269.8954986	58.7	9.0	2454580.8338639	86.26	2.48	2453190.64093	− 9.92	3.36
2455270.8623072	41.7	9.0	2454581.8459239	77.96	1.73	2453191.65473	− 5.91	3.56
2455349.7478270	4.7	9.0	2454724.4802846	− 117.74	1.27	2453551.62308	− 72.79	5.00
2455351.7263025	− 9.3	9.0	2454725.4983255	− 121.37	1.56	2454339.53949	134.00	4.93
2455352.7243194	3.7	9.0	2454726.4832450	− 120.54	1.57	2455001.70315	156.04	4.48
2455465.5203302	38.7	9.0	2455271.8407105	124.30	1.42			
2455466.5103888	25.7	9.0	2455649.7654997	− 73.82	2.01			
2455467.5077317	39.7	9.0	2455786.5492317	− 102.21	2.08			
2455468.4926389	32.7	9.0	2455787.4838577	− 93.49	1.66			
2455786.5547221	− 195.3	9.0	2455787.6993011	− 92.88	2.53			
2455787.5512296	− 190.3	9.0	2455788.4587689	− 86.93	1.92			
2455788.5404119	− 170.3	9.0	2455788.6109888	− 91.50	2.10			
2455968.8355111	100.7	9.0	2455788.7074614	− 83.90	3.01			
2455970.8644298	74.7	9.0	2455992.8338522	− 77.92	1.67			
2456034.8536087	− 19.3	9.0	2455993.7871396	− 80.38	2.00			
2456037.8611090	8.7	9.0	2455994.7989047	− 90.35	2.11			
2456160.5035894	15.7	9.0	2456063.7089752	250.12	3.48			
2456161.5099351	22.7	9.0	2456064.7231089	258.36	1.87			
2456164.5890537	55.7	9.0	2456183.4686863	223.49	3.03			
2456307.8687079	112.7	9.0	2456184.4750146	219.57	3.41			
2456308.8690886	117.7	9.0	2456442.7882798	95.12	2.19			
2456381.7577061	− 119.3	9.0	2456444.7375998	62.78	3.16			
2456463.6629499	− 189.3	9.0						
2456464.6620073	− 190.3	9.0						
2456554.5635006	144.7	9.0						
2456555.4998324	118.7	9.0						
2456676.8378428	− 0.3	9.0						
2456733.8400326	− 56.8	12.0						
2456734.7541033	− 50.8	11.0						
2456735.7646576	− 55.8	11.0						
2456736.8330743	− 47.8	12.0						
2456752.8898318	50.2	14.0						
2456754.7704681	76.2	13.0						
2456823.7610291	− 155.8	14.0						
2456824.7569383	− 181.8	14.0						
2456825.8288093	− 168.8	14.0						
2456881.6254682	130.2	14.0						
2456882.6396241	151.2	13.0						
2456883.5912828	149.2	13.0						
2457179.6595698	− 126.8	16.0						
2457180.6006537	− 127.8	15.0						
2457181.5978747	− 142.8	13.0						
2457182.5980141	− 120.8	13.0						
2457183.7046858	− 119.8	14.0						
2457184.6231976	− 111.8	13.0						

Table G8. HD152079.

CORALIE			HARPS			MIKE		
BJD	RV	Error	BJD	RV	Error	BJD	RV	Error
2455786.6489688	− 41.7	9.0	2454253.8065363	− 20.75	1.75	2452917.4972	− 24.3	6.2
2456463.6745808	14.3	9.0	2454367.5811986	− 22.95	1.00	2453542.6649	22.5	3.3
2456464.7049704	17.3	9.0	2454579.8264105	− 29.21	0.72	2453872.8022	− 8.5	2.5
2456465.6766024	8.3	9.0	2455649.8008277	− 30.70	1.01	2453987.5436	− 10.3	2.8
2456555.5745883	− 0.8	9.0	2455650.7595904	− 29.43	0.96	2453988.5202	− 12.6	2.7
2456676.8549118	2.2	15.0	2455651.8003619	− 29.35	0.84	2454190.8274	− 13.7	2.9
2456733.8533258	− 1.2	13.0	2455786.5261504	− 22.51	0.96	2454277.6950	− 19.7	3.4
2456734.8495354	− 17.2	11.0	2455787.5966780	− 22.46	0.85	2454299.6134	− 19.6	3.3
2456735.8130233	− 10.2	12.0	2455992.9178275	1.25	1.01	2454725.5353	− 35.1	2.6
2456736.8653294	7.8	15.0	2455993.8444865	3.09	0.93	2454925.9161	− 29.2	2.4
2456752.8688188	8.8	12.0	2456064.7106335	19.86	0.89	2454963.7753	− 22.6	2.7
2456754.7851172	0.8	14.0	2456184.5322797	44.23	0.93	2454993.7093	− 27.5	2.4
2456823.7916933	16.8	13.0	2456442.7259868	24.77	0.90	2455001.7291	− 25.3	2.9
2456824.7696220	− 3.2	13.0	2456443.7319729	27.81	1.62	2455017.6624	− 28.5	2.4
2456825.8154610	− 8.2	13.0	2456444.7714764	25.93	1.28	2455019.6938	− 22.5	2.2
2456881.6859346	10.8	13.0	2456462.7752093	19.99	1.30			
2456882.6527789	− 10.2	12.0	2456561.5772596	18.97	1.25			
			2456563.5044073	18.41	1.18			

Table G9. HD154672.

CORALIE			HARPS			MIKE		
BJD	RV	Error	BJD	RV	Error	BJD	RV	Error
2455268.8925184	− 51.4	9.0	2454367.5951401	225.90	0.69	2453189.71323	− 141.83	2.89
2455286.7126041	− 133.4	12.0	2454368.6185060	227.85	1.10	2453190.70833	− 143.62	2.73
2455286.7482435	− 137.4	12.0	2454578.8112608	82.73	0.61	2453191.72040	− 147.14	3.33
2455287.7447603	− 130.4	12.0	2454581.8703510	71.32	0.52	2453254.50616	175.30	2.60
2455287.7803973	− 136.4	12.0	2455271.8920649	− 18.52	0.63	2453596.68926	130.45	3.10
2455288.7337184	− 139.4	11.0	2455649.8248173	− 195.00	0.66	2453810.90968	− 5.00	2.56
2455288.7776633	− 138.4	12.0	2455786.5972307	− 87.04	0.66	2453872.81362	260.75	2.45
2455349.7906916	161.6	10.0	2455993.8674482	− 126.00	0.78	2454189.87086	− 80.09	3.62
2455350.8687367	177.6	10.0	2455994.8361631	− 98.02	0.83	2454189.87898	− 90.28	3.52
2455351.7067623	173.6	10.0	2456063.7424430	53.14	1.25	2454190.84022	− 57.35	2.84
2455352.7571340	172.6	9.0	2456064.7465191	50.37	0.66	2454215.86050	242.59	2.52
2455353.6007870	135.6	10.0	2456065.7448182	48.70	0.74	2454216.78927	243.77	2.54
2455354.6329905	151.6	10.0	2456183.5270912	188.65	0.85	2454217.87254	250.94	2.76
2455354.7244421	136.6	11.0	2456442.7630531	− 86.65	0.69	2454277.70250	67.40	2.74
2455355.6194464	135.6	11.0	2456443.7800510	− 86.90	1.29	2454299.62096	0.00	2.64
2455355.7115550	148.6	11.0	2456462.7983801	− 163.39	0.91	2454339.55738	− 145.72	4.15
2455433.5945428	− 58.4	11.0	2456462.8102434	− 164.91	1.02	2454501.89596	− 143.22	2.71
2455434.5939320	− 68.4	10.0	2456561.4986867	39.66	0.85	2455018.68932	213.92	2.17
2455467.5419737	− 152.4	11.0	2456563.5280947	36.30	0.89			
2455468.5360292	− 140.4	11.0						
2455786.6672674	− 128.5	10.0						
2456034.8785575	94.5	9.0						
2456037.8864541	86.5	9.0						
2456160.5115180	− 99.5	11.0						
2456161.5235072	− 68.5	12.0						
2456164.5556060	60.5	13.0						
2456381.7967325	47.5	10.0						
2456463.6867223	− 212.5	10.0						
2456464.7194041	− 226.5	10.0						
2456734.8670344	− 17.5	9.0						
2456735.8301098	− 20.5	9.0						
2456823.8058978	153.5	11.0						
2456825.8537984	178.5	11.0						
2456882.6789128	44.5	11.0						

Table G10. HD165155.

CORALIE			HARPS		
BJD	RV	Error	BJD	RV	Error
2455698.7379179	− 70.4	9.0	2454577.8573518	70.07	0.70
2455786.6994564	36.6	13.0	2454578.8259992	67.18	0.80
2455786.7108277	75.6	13.0	2454579.8512477	67.69	0.74
2455787.6641024	35.6	12.0	2455650.8171652	− 83.60	1.14
2455787.6754805	35.6	12.0	2455786.6216504	− 5.87	1.04
2455788.6765746	48.6	13.0	2455787.4979049	− 3.44	0.96
2455788.6875372	67.6	13.0	2455788.6355855	− 1.89	1.07
2456034.9332917	20.6	12.0	2455993.8895322	− 6.64	1.23
2456381.8066463	54.6	12.0	2455994.8596255	− 7.98	1.57
2456381.8190355	47.6	12.0	2456063.7543293	− 35.54	1.82
2456463.7613374	59.6	9.0	2456064.7595490	− 35.45	0.96
2456464.7345595	11.6	9.0	2456065.7693045	− 33.41	2.68
2456555.5907771	− 42.4	11.0	2456183.5412473	− 15.93	1.13
2456555.6041047	− 39.4	9.0	2456442.8006921	14.89	1.18
2456733.8878823	145.2	10.0	2456443.8064819	19.51	2.63
2456735.8673459	111.2	10.0	2456444.8081381	17.67	1.57
2456754.8071800	115.2	13.0	2456461.7756434	13.11	1.08
2456823.8481613	112.2	11.0	2456462.8238912	9.33	1.42
2456825.8695333	89.2	11.0	2456463.7557595	11.89	1.71
2456881.7083646	99.2	11.0	2456561.4867891	− 62.19	1.12
2456883.6490320	85.2	10.0			
2457077.8839217	120.2	13.0			
2457183.7828036	− 250.8	16.0			
2457184.6886555	− 250.8	15.0			
2457312.5069791	− 254.8	17.0			
2457318.4944200	− 279.8	16.0			

Table G11. HD224538.

CORALIE			HARPS			MIKE		
BJD	RV	Error	BJD	RV	Error	BJD	RV	Error
2455196.5457833	− 63.9	9.0	2454365.6728323	− 72.92	0.84	2453189.91295	− 2.66	2.86
2455197.5258897	− 62.9	9.0	2454724.7162997	87.00	0.93	2453190.91771	0.00	3.27
2455198.5268449	− 54.9	9.0	2454725.6845580	87.50	1.02	2453191.91314	7.12	2.85
2455352.9431841	− 89.9	9.0	2454726.6664725	89.44	0.65	2453254.73446	− 13.98	3.23
2455465.6728602	− 55.9	9.0	2454727.6026469	87.24	0.83	2454338.83927	3.92	3.86
2455468.6569334	− 51.9	9.0	2455786.8072676	− 5.84	0.80	2454339.75448	− 7.75	3.09
2455497.5904524	− 52.9	9.0	2455787.6269341	− 12.49	0.96			
2455514.6207088	− 42.9	9.0	2455787.8105224	− 16.34	0.73			
2455786.8585090	37.1	9.0	2455787.9313791	− 14.21	0.82			
2455787.8646502	25.1	9.0	2455788.5991810	− 14.30	1.26			
2455788.8218648	53.1	19.0	2455788.7826534	− 14.01	1.33			
2455877.6116650	93.1	22.0	2455883.5865245	46.83	1.19			
2455878.5958784	92.1	9.0	2455885.5121047	54.40	1.30			
2455879.6063410	108.1	9.0	2455885.5744505	52.39	1.53			
2455969.5203878	158.1	16.0	2455885.7033086	51.81	1.43			
2455970.5204393	167.1	16.0	2456064.9384446	67.21	0.85			
2456160.6541736	− 25.9	16.0	2456183.7248653	− 67.99	0.86			
2456164.7802416	− 4.9	16.0	2456185.6754003	− 70.76	1.02			
2456554.6541123	− 68.9	9.0	2456442.9267855	− 116.37	1.14			
2456554.6624176	− 54.9	9.0	2456461.8887446	− 110.55	1.03			
2456555.7132051	− 76.9	9.0	2456561.7050322	− 109.01	0.97			
2456675.5534417	− 27.9	16.0						
2456824.9242966	5.9	13.0						
2457317.6711775	− 3.1	36.0						

This paper has been typeset from a TEX/LATEX file prepared by the author.